Bioactive Materials 6 (2021) 4801–4815

Contents lists available at ScienceDirect

Bioactive Materials

journal homepage: www.sciencedirect.com/journal/bioactive-materials

# Fullerol-hydrogel microfluidic spheres for *in situ* redox regulation of stem cell fate and refractory bone healing

Jielai Yang, Jing Liang, Yuan Zhu, Mu Hu, Lianfu Deng, Wenguo Cui *, Xiangyang Xu **

*Department of Orthopedics, Shanghai Key Laboratory for Prevention and Treatment of Bone and Joint Diseases, Shanghai Institute of Traumatology and Orthopaedics, Ruijin Hospital, Shanghai Jiao Tong University School of Medicine, 197 Ruijin 2nd Road, Shanghai, 200025, PR China*

ARTICLE INFO

*Keywords:*
Microfluidics
Fullerol
Reactive oxygen species
Stem cell
Refractory bone healing

ABSTRACT

The balance of redox homeostasis is key to stem cell maintenance and differentiation. However, this balance is disrupted by the overproduced reactive oxygen species (ROS) in pathological conditions, which seriously impair the therapeutic efficacy of stem cells. In the present study, highly dispersed fullerol nanocrystals with enhanced bioreactivity were incorporated into hydrogel microspheres using one-step innovative microfluidic technology to construct fullerol-hydrogel microfluidic spheres (FMSs) for *in situ* regulating the redox homeostasis of stem cells and promoting refractory bone healing. It was demonstrated that FMSs exhibited excellent antioxidant activity to quench both intracellular and extracellular ROS, sparing stem cells from oxidative stress damage. Furthermore, these could effectively promote the osteogenic differentiation of stem cells with the activation of FoxO1 signaling, indicating the intrinsically osteogenic property of FMSs. By injecting the stem cells-laden FMSs into rat calvarial defects, the formation of new bone was remarkably reinforced, which is a positive synergic effect from modulating the ROS microenvironment and enhancing the osteogenesis of stem cells. Collectively, the antioxidative FMSs, as injectable stem cell carriers, hold enormous promise for refractory bone healing, which can also be expanded to deliver a variety of other cells, targeting diseases that require *in situ* redox regulation.

## 1. Introduction

Restoration of extensive bone loss and defects remains a challenge in modern society, and difficulties are enhanced when in the condition of aging and other diseases (*e.g.* diabetic or osteoporosis), which make refractory bone healing an intractable medical issue that seriously jeopardizes an individual's health worldwide [1]. In these diseased conditions, oxidative stress occurs and induces the production of excess ROS that destroys the redox balance, which in turn results in the structural damage and dysfunction of stem cells [2,3]. At present, mesenchymal stem cell (MSC) transplantation is one of the most promising approaches for bone tissue engineering. However, the low delivery efficacy and low retention of MSCs in these defects hamper its clinical application [4]. The delivery of stem cells *via* hydrogel microspheres provides an appealing strategy for tissue engineering, which has significant advantages over conventional bulk hydrogel *(e.g.* flexible in injectability and optimization of the cell maintenance microenvironment) [5,6]. However, the ROS microenvironment of diseased conditions not only impairs the regenerative potential of inherent stem cells but also reduces the therapeutic efficacy of implanted stem cells in the impaired areas [7,8]. The excessive ROS and, or insufficient antioxidant agents make these defects difficult to heal [9]. Hence, novel strategies for manufacturing antioxidative hydrogel microspheres as stem cell carriers to promote bone regeneration in the ROS microenvironment are urgently needed for the clinical therapeutics of refractory bone healing.

The combination of a crosslinkable hydrogel network with functional nanoparticles (NPs) can provide preferable functionality to the composite material [10,11]. Gelatin methacryloyl (GelMA) has been extensively used in the application of tissue engineering due to their inherent bioactivity and tunable physicochemical properties [12]. The chemical properties of GelMA can be easily regulated by adjusting the ratio of gelatin and merhacryloyl. From the processing perspective, GelMA can form photo-crosslinkable hydrogels with tailorable mechanical properties. Fullerol, which is a powerful antioxidant, is one of the C60 derivatives [13]. Compared with other carbon nanomaterials (*i.e.* carbon

Peer review under responsibility of KeAi Communications Co., Ltd.
* Corresponding author.
** Corresponding author.
*E-mail addresses:* wgcui80@hotmail.com (W. Cui), xu664531@126.com (X. Xu).

https://doi.org/10.1016/j.bioactmat.2021.05.024
Received 14 April 2021; Received in revised form 7 May 2021; Accepted 7 May 2021

nanotube and graphite), fullerol has a much lower cytotoxicity [14]. As one of the most exploited properties in biomedical study, the antioxidant performance of fullerol largely depends on the hydroxyl groups and their location on the C60 sphere [15]. Although the specific mechanism of fullerol in quenching ROS is not completely understood, the mainstream "cage capturing" theory holds that ROS adheres to the electron-deficient fullerol surface *via* π-π interactions, and are destroyed by transferring electrons to the inner cage, which is similar to the ROS quenching of superoxide dismutase [8,16]. By quenching excessive ROS in pathological conditions, fullerol exhibits an excellent therapeutic effect towards bacterial infection [17], chemotherapy side effects [18], and acute myocardial infarction [19]. In the musculoskeletal system, fullerol prevents the degeneration of the intervertebral disk [20] and articular cartilage [21]. More importantly, the antioxidative fullerol promotes osteogenesis [22] and inhibits osteoclastogenesis [23], suggesting its tremendous potential of application in bone tissue engineering. Physically, the water solubility of fullerol reinforces due to the presence of multiple hydroxyl groups, which is favorable for preparing the homogeneous hydrogel [24]. However, due to the big size and high rigidity of the C60 sphere, fullerol in aqueous solutions tends to self-assemble into aggregates with different structures and sizes [25,26]. Upon the aggregation of C60 spheres, hydrophobic domains are formed, resulting in a reduced surface area available to react, which may weaken their biochemical performance in the aqueous solution [27]. Therefore, it is extremely vital to optimize the fullerol-in-GelMA hydrogel system to maximize its biological efficacy.

With a narrower particle-size distribution and higher reproducibility, microfluidic technology has a significant advantage in preparing monodisperse hydrogel microspheres with suitable size, which is essential for maintaining a microenvironment that favors cell survival [28–30]. More importantly, compared with bulk synthesis methods (*e.g.* sonication and static mixer), the microfluidics method, which controls the solvent flow rates, heat transfer efficacy, channel length and geometry, can effectively produce smaller nanoparticles with a narrower size distribution [31,32], and this can be used to promote the fullerol reactivity. Using microfluidic technology, both monodisperse hydrogel microspheres and highly dispersed fullerol nanocrystals can be achieved at the same time. Hence, the optimization of the fullerol-in-GelMA hydrogel system *via* fabricating GelMA hydrogel microspheres containing highly dispersed fullerol nanocrystals is not only conducive for the better delivery of stem cells, but also improves the biochemical reactivity of fullerol, which should be a promising strategy for bone healing in the ROS microenvironment. In general, there are two strategies to deliver cells using microfluidic spheres, *i.e.* in the microsphere and on the microsphere. Compared to the "in the microsphere" strategy, the "on the microsphere" strategy generates microspheres before cell ingrowth, providing more flexibility in the choice of gelation conditions and precursor solution. Furthermore, cells "on the microspheres" proliferate faster than that in the inner space of microspheres, since space is not tightly confined [33,34].

In the present study, highly dispersed fullerol nanocrystals with enhanced bioreactivity were incorporated into GelMA microspheres using one-step innovative microfluidic technology to construct fullerol-hydrogel microfluidic spheres (FMSs) for *in situ* regulating the redox homeostasis of stem cells and promoting refractory bone healing (Fig. 1). The fullerol nanocrystals were firmly immobilized within hydrogel microspheres *via* both the physical entanglement of hydrogel matrix [10] and non-covalent interactions (*e.g.* hydrophobic and π-π binding) between the GelMA and the C60 sphere surface [35]. Initially, the biocompatibility and antioxidant activity of FMSs were investigated to demonstrate that they could effectively quench ROS to create a favorable microenvironment for survival of bone marrow mesenchymal stem cells (BMSCs). Furthermore, the *in vitro* osteogenic differentiation of BMSCs was analyzed to validify the intrinsically osteogenic property of FMSs. Finally, the *in vivo* bone healing effect were investigated *via* implanting BMSCs-laden FMSs into a rat cranial bone defect model.

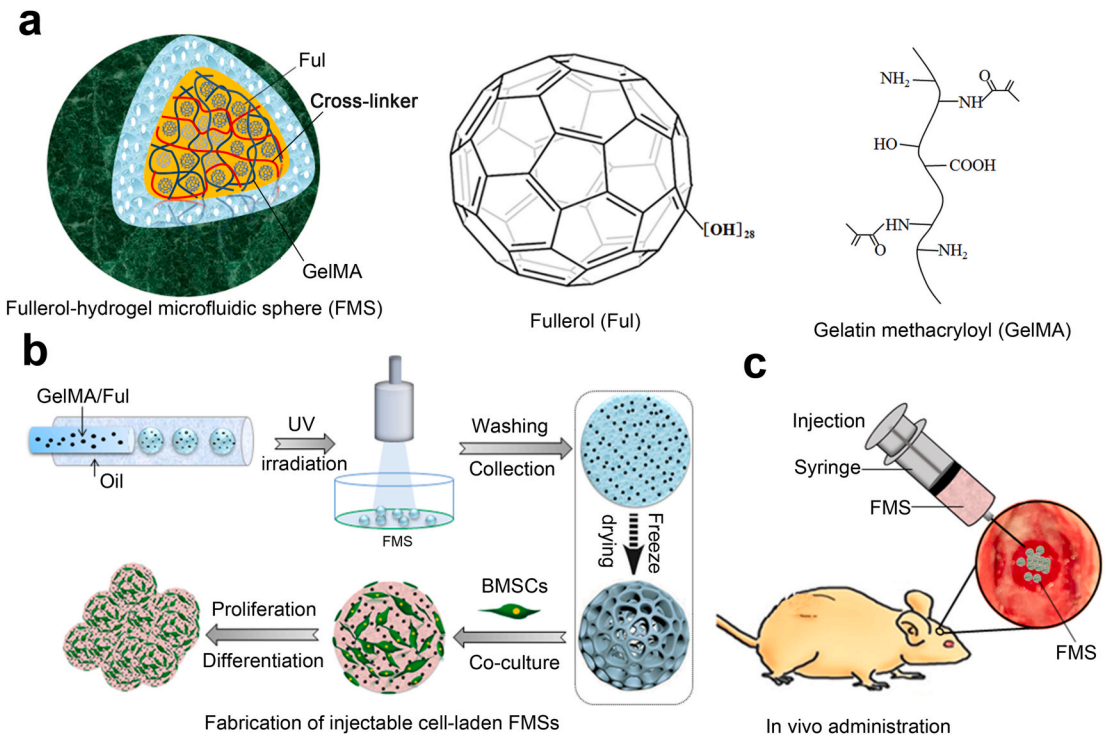


**Fig. 1.** a) Schematic of the three-dimensional structure of FMSs, molecule structures of fullerol, and gelatin methacryloyl (GelMA). To show the three-dimensional structure, the hydrogel matrix network of FMS are rendered into different colors. The fulerol was immobilized within the GelMA microspheres by both the physical entanglement of hydrogel matrix network and the noncovalent interactions between GelMA and fullerol. b) Schematic illustrations of the FMSs fabrication, and the growth and differentiation of BMSCs on FMSs. The freeze-drying process, indicated by dotted arrow, was performed to show porous structure of FMSs and the wet (non-lyophilized) FMSs were used for cell culture. c) The *in vivo* bone repair schematic of BMSCS-laden FMSs in a rat calvarial defect model.

## 2. Materials and methods

### 2.1. Materials

All reagents were obtained from Sigma-Aldrich, unless noted otherwise. Fullerol nanoparticles ($C60[OH]_{28}{\cdot}17H_2O$, 99.5% purity) were obtained from Tanfeng Graphene Technology Co., Ltd. (Suzhou, China).

### 2.2. GelMA synthesis

GelMA was synthesized according to the method that reported in our previous study [36]. Briefly, the 10% (w/v) gelatin was completely dissolved into Dulbecco's phosphate-buffered saline (DPBS) (Invitrogen) at 60 °C. The methacrylic anhydride (MA) (0.8 mL per *g* gelatin) was supplemented to react with gelatin at 50 °C under staring for 2 h. The reaction was stopped by supplementing additional DPBS (5-fold dilution). The diluted solution was dialyzed in distilled water at 40 °C for 1 week. Afterwards, the purified solution was freeze-dried 1 week, forming a white foam that could be long-term stored at −80 °C.

### 2.3. Microfluidic generation of GelMA-Fullerol microspheres

In order to prepare the prepolymer solution, fullerol at different concentrations (0, 1, 10, 100, and 200 μM) were supplemented into the 5 wt% GelMA solution containing 0.5 wt% photoinitiator. Then, the mixture was then sonicated for 30 min at 55 °C, forming a homogeneous solution. In order to fabricate the GelMA-Fullerol microspheres, the prepolymer solution was employed as the dispersed phase, and the continuous phase contained paraffin oil with 5 wt% Span80. These two phases were injected into different microchannels and the flow rates of them were fine-tuned by syringe pumps to obtain the monodisperse droplets (<200 μm). The collected emulsion droplets were photopolymerized for solidification under UV irradiation (365 nm, 5 min). In order to remove the excessive additives, including paraffin oil and photoinitiator, the microspheres were thoroughly extracted in cleansing water, and then purified in phosphate buffer saline (PBS). The resulting microspheres were imaged using an optical microscope, and their particle sizes were analyzed using Image J software.

### 2.4. Physical characterization of GelMA-Fullerol microspheres

(I) Scanning Electron Microscopy (SEM): The surface morphology of the hydrogel microspheres was examined by a SEM (S-4800; Hitachi, Kyoto, Japan). Lyophilized hydrogel microspheres were added on the conductive adhesive and were spray-coated with gold. (II) Laser Scanning Confocal Microscopy (LSCM): The surface morphology of the hydrogel microspheres *was examined by LSCM* (ZEISS, Axio, Germany). Alizarin Red and Calcein were added to stain the hydrogel microspheres, respectively. After freeze-drying, the hydrogel microspheres were monolayer dispersed on a confocal dish. The Alizarin Red staining revealed the morphology of the hydrogel microspheres in red, while the Calcein staining revealed the morphology of the hydrogel microspheres in green. (III) Transmission Electron Microscope (TEM): The morphology of the fullerol nanoparticles within the hydrogel microspheres and in the degradation solution was, respectively, investigated under a high resolution TEM (H-7500, Hitachi Ltd. Japan). For the former, hydrogel microspheres were rapidly dissolved with collagenase type II (10 U $mL^{-1}$), and the lysed solution that contained the fullerol nanoparticles was dropped onto holey-carbon film-supported grids and imaged under TEM (IV). Degradation analysis: By mimicking the physiological environments [37], 0.5 mL of hydrogel microspheres were incubated with 0.5 ml of type II collagenase (0.1 U $mL^{-1}$)-containing PBS (pH 7.4) in 1.5-mL tubes at 37 °C for 5 weeks. The investigation was continued by monitoring the pH value and replenishing the equal amount of collagenase-containing PBS every week. At the predetermined time points, the hydrogel microspheres were subjected to several analyses, including microscopic observation and residual weight measurement. For the latter, after washing with deionized water, the hydrogel microspheres were freeze-dried for weighting. The degradation rate (DR) was calculated, as follows:

$$DR(\%) = \frac{W_o - W_t}{W_o} \times 100\% \quad (1)$$

(Wo refers to the initial weight, and Wt refers to the weight at time t)

### 2.5. Biocompatibility of GelMA-Fullerol microspheres

(I) Cell Culture: The BMSCs of Sprague Dawley (SD) rats were purchased from Cyagen Biosciences (Suzhou, China) and were cultured on hydrogel microspheres in Dulbecco Modified Eagle Medium, supplemented with 10% fetal bovine serum (Gibco), 100 μg·mL-1 of streptomycin (Gibco) and 100 U·mL-1 of penicillin (Gibco) in an incubator at 37 °C with 5% CO2. The hydrogel microspheres were dispersed in the medium for 24 h to form medium-containing hydrogel microspheres, which were mixed with fresh medium in different ratios (v/v) to prepare the solution for the BMSCs culture. The culture media was exchanged every 3 days. (II) Cell Viability: At day 3, 7 and 14, the cell viability was examined to determine the BMSCs survival on the hydrogel microspheres at different fullerol concentrations (0, 1, 10, 100, and 200 μM). Then, $1 \times 10^5$ BMSCs were mixed with 300 μL of 33.3% (v/v) microgel solution (V[microgel]:V[total] = 1:3) in 48-well tissue culture plates. At day 3, 7 and 14, the cell viability was measured using a live/dead cell staining kit (Life Tech, US), which stained the live cells with calcein-AM (green) and stained the dead cells with ethidium homodimer-1 (red). Next, cells were stained at room temperature for 20 min and then observed under LSCM. At day 14, these cells were successively labelled with phalloidin (5 μg $mL^{-1}$) (Life Tech, US) and DAPI (10 μg $mL^{-1}$) (Life Tech, US) for 20 min, and 10 min at room temperature, respectively. The positively labelled cells were detected using LSCM. (III) Cell Proliferation: In order to exclude the interference effect that from the deposited cells on the culture plate, the cell-laden hydrogel microspheres were transferred to a new plate for the test. At day 1, 4, and 7, the proliferation capability of BMSCs was detected by the CCK-8 assay. After incubation with 10% CCK-8 solution (Beyotime, China) for 2 h, the resulting solution absorbance was detected using a microplate reader (Tecan, Switzerland) at a wavelength of 450 nm. All samples were tested in triplicate.

### 2.6. Antioxidant activity of GelMA-Fullerol microspheres

(I) Total Antioxidant Capability (TAOC) Assay: TOAC was measured using a rapid ABTS test (Beyotime, China). Briefly, the peroxidase solution (20 μL), sample/Trolox standard (10 μL) and ABTS solution were successively added into a 96-well-plate. Then, the mixed solution was incubated for 5 min at room temperature, and detected at 414 nm wavelength. (II) Intracellular ROS Detection: In order to induce the oxidative stress of stem cells, $H_2O_2$ was used at a concentration of 100 μM, which was consistent with a previous study [8]. BMSCs-laden hydrogel microspheres with different fullerol concentrations (0, 1, 10 μM) were incubated with $H_2O_2$ for 2 h. Following $H_2O_2$ treatment, the intracellular ROS was measured using a ROS Assay Kit (Beyotime, China). Briefly, $H_2O_2$-treated BMSCs were incubated with DCFH-DA (10 μM) at 37 °C for 20 min, washed with PBS for three times, and stained with DAPI (10 μg/mL). The positively stained cells were detected by LSCM. The fluorescence intensity of DCFH-DA was detected at 525 nm emission wavelength and 488 nm excitation wavelength, and then quantified using Image J software. (III) Live/dead staining: As mentioned above, the BMSCs-laden hydrogel microspheres were incubated with $H_2O_2$ (100 μM) for 12 h and 24 h, and the cell viability of BMSCs was detected. The labelled cells, including green live cells and red dead cells, were detected by LSCM. The stained cells were quantified

using the Image J software. The following equation was used to calculate the cell viability:

$$\text{Cell viability}(\%) = \frac{\text{The amount of live cell}}{\text{The amount of total cell}} \times 100\% \quad (2)$$

### 2.7. Osteogenic activity of GelMA-Fullerol microspheres

(I) Alizarin Red S staining: BMSCs-laden hydrogel microspheres with different fullerol concentrations (0, 1, and 10 μM) were incubated with growth or osteogenic media in a 24-well-plate. At day 7 and 14, cell-laden hydrogel microspheres were stained with Alizarin Red S dye (Solarbio, China) according to the instructions. The stained samples were imaged using an optical microscope and digital camera, respectively. After dissolving the mineralized extracellular matrix with 10% acetic acid, the OD values of the solution at wavelength 405 nm were measured to quantify the Alizarin Red S staining. (II) Alkaline Phosphatase (ALP) staining: At day 4 and 7, the cell-laden hydrogel microspheres were stained using a ALP staining kit (Beyotime, China). The stained cells were imaged using an optical microscope and digital camera, respectively. After the lysing of cells with RIPA lysis buffer, the ALP activity was obtained by measuring the OD value in the supernatant at 405 nm wavelength. The value was normalized to the total protein detected at 560 nm wavelength using a BCA Protein Assay Kit (Thermo Scientific, US). (III) Immunofluorescence Staining: At day 7, cells were fixed with 4% paraformaldehyde. After overnight incubation with the primary rabbit anti-OCN (Abcam), anti-BMP2 (Abcam) and anti-COL1A1 (Abcam) at 4 °C, these cells were incubated with the FITC-conjugated secondary antibody (Servicebio, China) for 1 h at room temperature. Then, the cell nuclei was stained with DAPI (Life Tech, USA) in the darkness for 15 min. Subsequently, these stained cells were observed by LSCM. (IV) Quantitative real-time PCR (qRT-PCR) analysis: At day 7, the cells were harvested. The total RNA was extracted using RNAiso Reagent (Takara, Japan), and reverse-transcribed into cDNA using the PrimeScript® RT reagent Kit (TakaRa, Japan). Afterwards, the RT-RCP was conducted using the a 7500 Fast Real-Time PCR system (Applied Biosystems, US) with the SYBR® Green Assay kit (TakaRa, Japan). The primer sequences are listed in Table S1. The expression levels of genes were determined using specific primers, and normalized to β-actin. (V) Western blot: The primary rabbit anti-FoxO1(Abcam), anti-SOD2 (Abcam) and mouse anti-β-Actin (Life Tech) were used in the test. The total protein was extracted from the collected cells using the BCA protein assay kit (Thermo Scientific, USA). After the protein transferring, and membrane blocking and washing, the primary antibodies were used to incubated with the membranes at 4 °C overnight. Then, the secondary antibody (Life Tech) was used to incubate with the membrane for 1 h at room temperature. The proteins labelled on the membrane were detected using the ChemiDoc Imaging Systems (Bio-Rad, USA).

### 2.8. In vivo bone repair via BMSCs-laden GelMA-Fullerol microspheres

(I) Rat calvarial defect model and BMSCs-laden hydrogel microspheres implantation: The calvarial defect model of SD rats (300 ± 10 g) was used to study the osteogenic effect of BMSCs-laden hydrogel microspheres. The *in vivo* experiment was approved by the Animal Ethics Committee of Ruijin Hospital Affiliated to Shanghai Jiao-Tong University School of Medicine. The calvarial defect model was prepared as previously described [38]. Briefly, the parietal bone was exposed through a midline incision from the bipupillar line to the occipital. Using an electric drill, the critical-size defects with a 5-mm diameter were randomly generated on the unilateral parietal bone. These rat models were divided into four groups (n = 6, per group): (a) blank, (b) BMSCs, (c) GelMA microspheres + BMSCs, (d) GelMA-Fullerol microspheres + BMSCs. BMSCs ($1 \times 10^7$ cells $mL^{-1}$) were resuspended in PBS, GelMA microspheres and GelMA-Fullerol microspheres (the concentration of the microsphere was 50% [v/v], $C_{Ful}$ = 10 μM, 0.035 wt% in respect to GelMA). These mixtures (100 μL) were rapidly injected into these calvarial defects using a 24-gauge needle. PBS was given to the blank group. (II) Micro-CT evaluation: At 8 weeks after surgery, the calvarial bones were collected, fixed with 10% paraformaldehyde solution, and evaluated using micro-CT (Scanco Medical, Switzerland). The current was 130 μA, and the voltage was 70 kV. The specimens were further analyzed using the Scanco software. The entire defect area was semi-automatically selected as the region of interest (ROI), and the bone volume fraction (bone volume [BV]/total volume [TV]) and bone mineral density (BMD) of the ROI were analyzed using this software. (III) Histological evaluation: After the micro-CT scanning, the fixed samples were decalcified, paraffin-embedded, and sliced for H&E staining. The morphology and new bone were observed under the microscope. (IV) Immunohistochemical Analysis: For immunohistochemical examination, the samples were permeabilized with Triton X-100 (0.3%, 10 min), blocked with goat serum (5%, 30 min), and then incubated with the primary antibody at 4 °C overnight. The primary antibodies included rabbit anti-FoxO1(Abcam; Ref. s1), anti-SOD2 (Abcam; Ref.s2), anti-OCN (Abcam; Ref.s2), and anti-BMP2 (Abcam; Ref.s3). After the incubation with the primary antibody, the secondary antibody was used to incubated with the samples at room temperature for 1 h. The staining was developed using the diaminobenzidine tetrachloride. Finally, the positively stained cells were observed under a microscope, and quantified by Image J software.

### 2.9. Statistical analysis

All data were expressed as mean ± SD. The two-tailed non-paired Student t-test was employed for comparisons between two groups. $P < 0.05$ was considered statistically significant.

## 3. Results and discussion

### 3.1. Microfluidic synthesis of FMSs containing highly monodispersed fullerol nanocrystals

The physicochemical properties of the fullerol was verified in **Figure S**1a-**S1**d, and the fullerol with multiple hydroxyl groups (n~28) (Fig. S2) exhibited excellent water solubility (Figs. S1e and S1f). Spherical FMSs were prepared using a microfluidic flow-focusing device, which is suitable for the high throughput fabrication of highly monodisperse microspheres with suitable size [34]. Aqueous FMSs were initially presented in emulsion drops of water-in-oil (W/O) (Fig. 1b). Fullerol mixed with 5 wt% GelMA containing 0.5 wt% photoinitiator were used as the aqueous phase, while the oil phase consisted of paraffin oil and 5 wt% span80. The 5 wt% GelMA was used based on the fact that concentrations below 4% hinders hydrogel formation, while concentrations exceeding 8 wt% inhibited the cell growth in the hydrogel [39]. Both flow rates at the aqueous phase (Qa) and oil phase (Qo) affected the particle size of microspheres. By tuning these two phases ratios (Qa: Qo = 1/6–1/10), FMSs with a diameter between 140 μm and 170 μm were obtained (Fig. 2c and d). The size falls within the ideal microsphere size range (100–300 μm), which is beneficial for good growth of BMSCs [40]. The porous surface topography of the microcarriers increased surface area for cell attachment (microporous), and provided multiple internal pores for cell ingrowth (macroporous) [41]. In order to investigate the surface morphology of these FMSs, the FMSs were instantly fixed in liquid nitrogen at ultra-low temperature, and lyophilized. Through this process, the morphology of the FMSs was preserved to a large extent, which is close to that in the hydrated state. As shown in Fig. 2a, the surface pores of FMSs range from a few microns to dozens of microns (2.9–34.3 μm), which is suitable for cell attachment. However, due to the soft and fragile properties of FMSs (<200 μm), the structures of most FMSs were destroyed during the sample preparation process for the SEM examination. In order to address this, the dye-labelled FMSs were

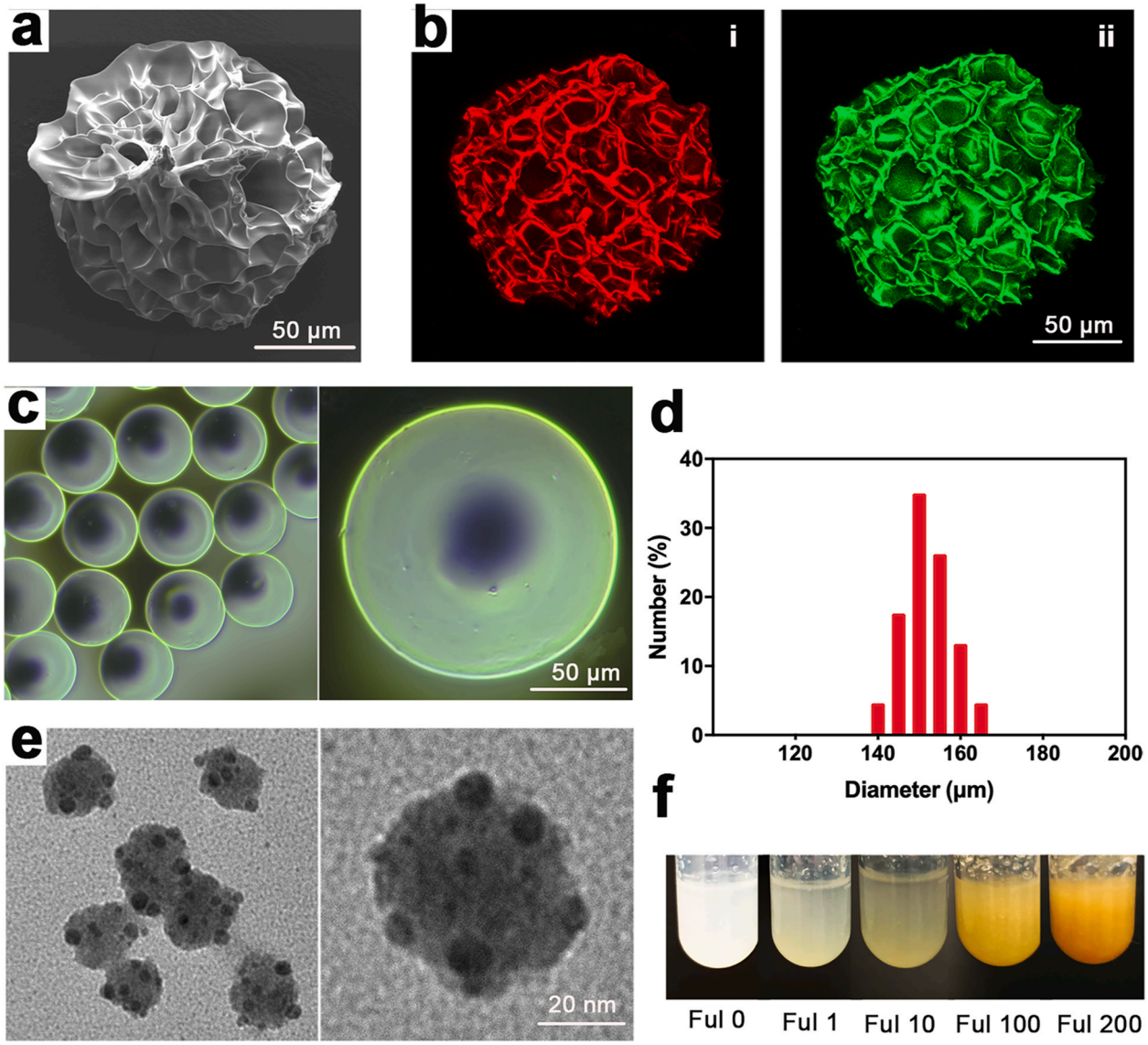


**Fig. 2.** Characterization of FMSs ($C_{Ful}$ = 10 μM, 0.035 wt% in respect to GelMA). a) SEM image of FMSs. b) The LSCM image of FMSs embedded with Alizarin Red (i) and Calcein (ii). The Alizarin Red and Calcein were incorporated into GelMA pre-solution, and then solidified into dye-labelled FMSs *via* photopolymerization. c) The Optical Microscopy (OM) image of FMSs. d) The particle size distribution of FMSs. e) The TEM image of fullerol nanocrystals within FMSs. The FMSs are degraded *via* collagenase and the exposed fullerol nanocrystals in the aqueous solution were detected using the TEM. f) The photograph of deposited FMSs with different concentrations of fullerol (0, 1, 10, 100, and 200 μM) in the aqueous solution.

further observed under LSCM, in which the structure of most FMSs were intact. The results were similar to that of SEM detection, which again confirms the porous surface morphology of FMSs (Fig. 2b). Once formed, the FMSs with diameters of less than 200 μm can be easily injected through a 24-gauge syringe head, which is suitable for *in situ* minimally invasive tissue repair (Fig. 1c). Fullerol is highly water soluble due to the presence of abundant hydroxyl groups on the surface. However, the hydrophobic nature of the aromatic carbon cage enables these to self--assemble in the aqueous solution, forming larger aggregates with diameters of hundreds of nanometers [42,43]. The structure and size of the nanoparticle in the suspension varies according to the hydrodynamics as well as the solution conditions [44]. Using the microfluidic device, highly monodispersed fullerol nanocrystals with a smaller size (average diameter of approximately 40 nm) were obtained (Fig. 2e). Under this condition, the curvature of fullerol nanocrystals increased to obtain a larger exposed surface area of the C60 sphere, which may be beneficial for fullerol-related biological applications [27]. Theoretically, hydrogel microspheres with nanoscale-sized network pores are ready to stabilize nanoparticles within their matrix, forming composite microspheres with additional functionalities [10,45]. In addition, the hydrophobic and π-π interactions between the GelMA and the C60 sphere surface further immobilize fullerol within the microspheres (Fig. 1a) [35]. The produced FMSs can be dispersed into a homogeneous supennsion *via* gentle shaking, and completely precipitated after a few minutes standing, with a clear supernatant, while the deposited FMSs would be colored (Figs. S3a and S3b). The state can remain unchanged over a month in PBS at 4 °C, which is indicative of the structural stability of FMSs and the retention of fullerol within FMSs (Fig. S3c) The deposited pure GelMA microspheres are translucent by visual inspection, while the color of deposited FMSs deepens with the addition of fullerol (Fig. 2f), which is similar to that of fullerol solutions [46].

### 3.2. *Degradation behavior of FMSs and morphological change of dissociated fullerol nanocrystals*

In order to assess the ability of the FMSs as stem cell carriers for bone

healing, the degradation performance was investigated. A previous study investigated GelMA hydrogel degradation using 2 U $mL^{-1}$ of collagenase solution [39]. However, the FMSs rapidly degraded within a few hours under this condition, which was probably due to the larger surface-area-to-volume ratio, when compared to the bulk hydrogel. In fact, this process was too quick to be observed in the dynamic changes of microspheres *in vitro*, and this can hardly represent the gradually degradation process *in vivo* in much lower collagenase conditions. By mimicking the *in vivo* healing environment [37], FMSs were incubated in PBS containing collagenase with a much lower concentration (0.1 U $mL^{-1}$) for five weeks (Fig. 3a). It was observed that fine degradation particles appeared on the surface of FMSs within the first week. At week two, the marginal structure of FMSs started to collapse with increased cracks. The number of existing FMSs dropped at week three, and the FMSs completely disappeared at week five. In addition, the particle size tended to increase over time, which is indicative of bulk degradation. Overall, the FMSs degradation was a slow, progressive, and dynamic process. The residual weight of FMSs decreased with time, which was consistent with the morphological change (Fig. 3b). With the complete FMS degradation, the final residual component should be fullerol (~0.035 wt%), which, however, could hardly be precisely measured using the weight method, and was neglected. Beyond the changes in the body frame of FMSs, the change in fullerol nanocrystals was also investigated. After the FMSs degradation, the immobilization effect of fullerol nanocrystals was destroyed and the split fullerol nanocrystals could diffuse to the surrounding aqueous solution due to concentration-gradient effect. Of course, it couldn't exclude the capture of a small amount of split fullerol nanocrystals within the remaining FMSs. Over a period of 5 weeks, the split fullerol nanocrystals in lysis supernatant turned into larger particles (average diameter of approximately 200 nm) (Fig. 3c), which was similar to those directly formed in the aqueous solution (Fig. S1d). The underlying mechanism of this change may be the growth of the nanocrystal itself and/or the coalescence of nanocrystals. On the one hand, the fullerol in the aqueous solutions tended to self-assemble into large aggregates due to the big size and high rigidity of the C60 sphere [26]. On the other hand, the nanoparticles grew in the solution based on the mechanisms of the surface reaction and the monomer's diffusion to the surface [47].

### 3.3. Survival and proliferation of BMSCs on FMSs

Cell culturing on the hydrogel microspheres exhibits obvious advantages, when compared to the conventional plate culturing system [34]. Due to their larger surface-to-volume, hydrogel microspheres take less substrates to culture more cells. In addition, the three-dimensional culture using hydrogel microspheres are more closely to that in the *in vivo* conditions, and hydrogel microspheres can be used as cell carriers for minimally invasive tissue repair. The fullerol nanocrystals, which gradually exposed following FMSs degradation, could directly contact *in situ* with and be taken up by the cells. Previous studies have demonstrated the dose-dependent cytotoxicity of water-soluble fullerene on several cells [48]. In fact, the cytotoxicity varied in different cells due to various factors (*e.g.* cell type, the dissolving medium, aggregation of nanoparticles, and group number of fullerene derivatives), and the cell type was considered as the most significant factor that influenced the cytotoxicity of fullerene and its derivatives [49,50]. However, most previous studies have investigated the toxicity of fullerol in the aqueous solution, which might be different from that in the hydrogel. In order to investigate the viability of BMSCs seeded on FMSs with different concentrations of fullerol, the live/dead cell assay was employed for the quantification of live cells and dead cells (Fig. 4a). The results revealed that BMSCs maintained better viability on FMSs that contain 0, 1 and 10

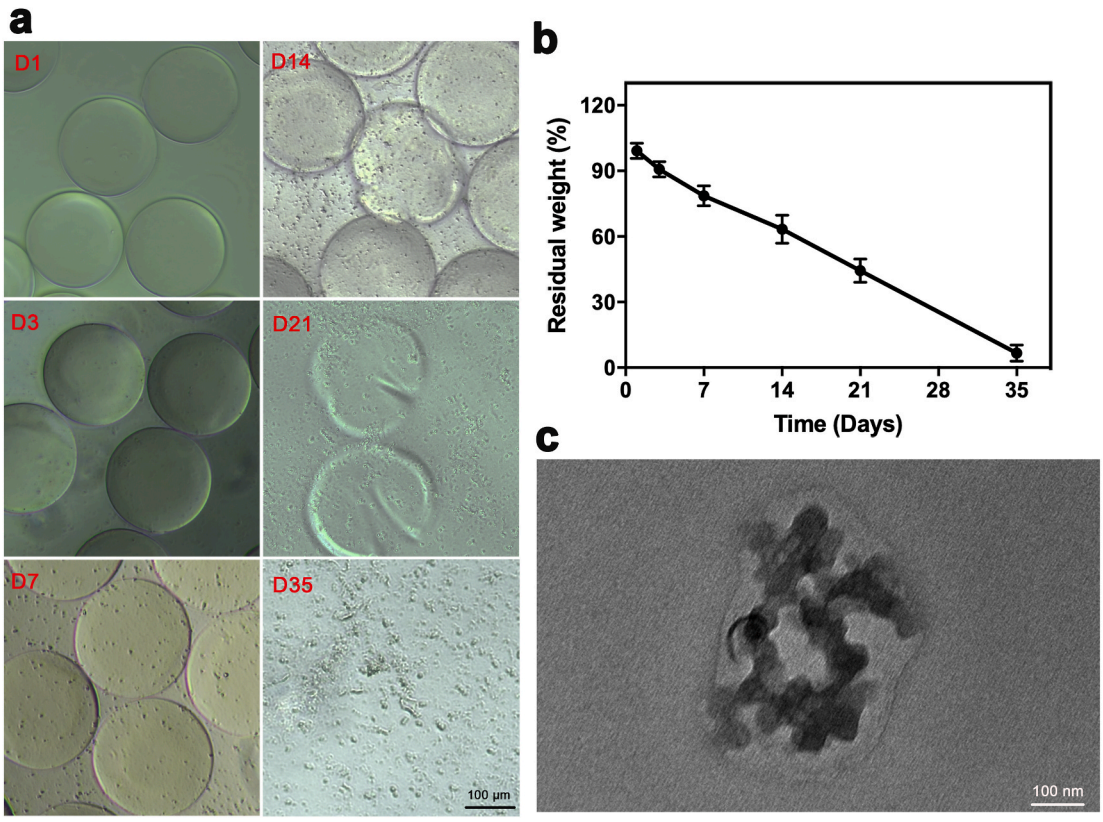


**Fig. 3.** Degradation analysis of FMSs incubated with the collagenase ($C_{Ful}$ = 10 μM, 0.035 wt% in respect to GelMA). a) The OM images showing morphological changes of FMSs over 5 weeks. The fine particles around FMSs increased in the early stage (D3-D7), and cracks (D24) and fractures (D21) of FMSs were observed in the late stage. b) The residual weight of FMSs (n = 3). The final residual component was fullerol (~0.035 wt%). c) The TEM image of fullerol nanocrystals in the degradation solution after 5 weeks.

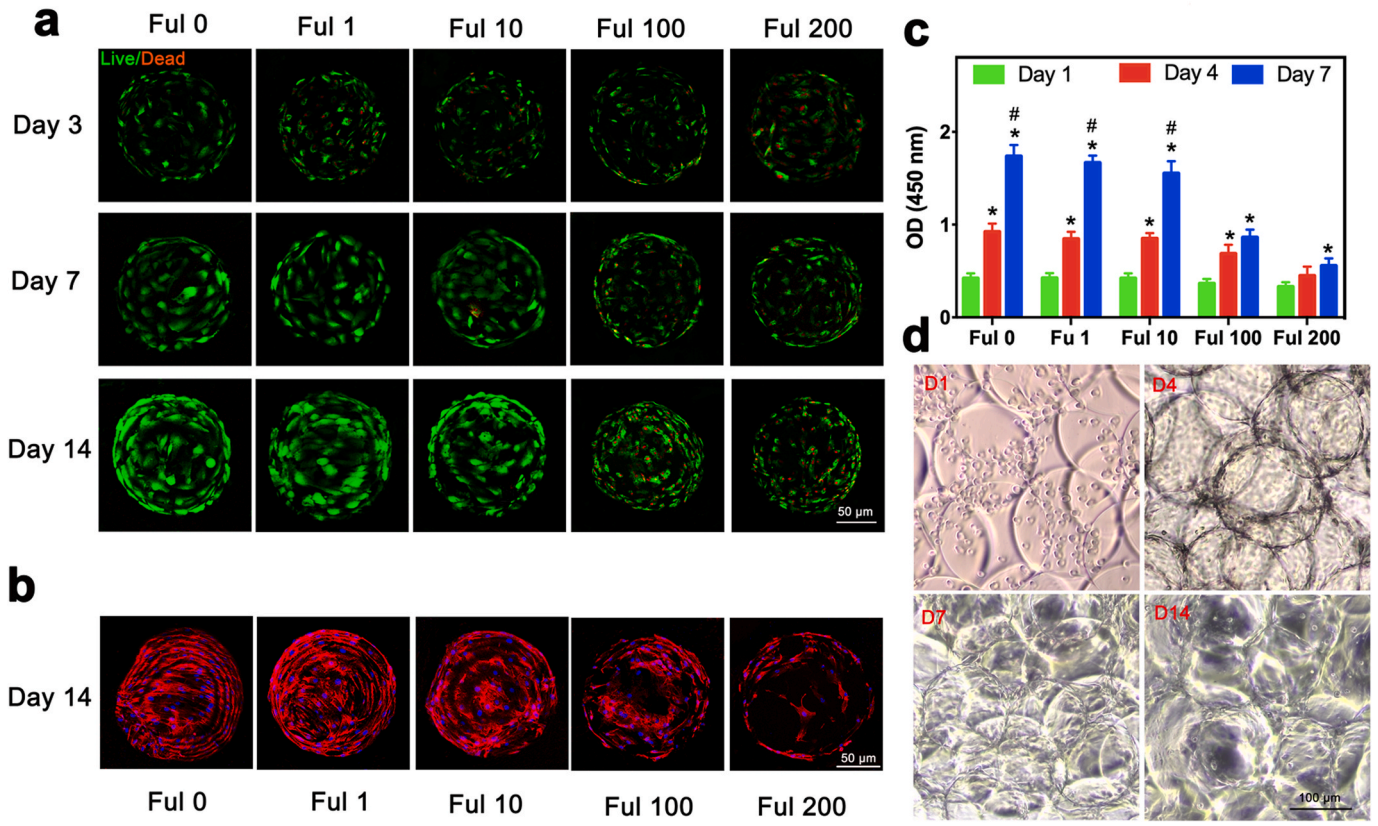


**Fig. 4.** Cytocompatibility of FMSs. a**)** The live/dead staining images of BMSCs seeded on monodispersed FMSs at day 3, 7, and 14. The live cells are in green, and the dead cells are in red. b) The LSCM images of BMSCs seeded on monodispersed FMSs at day 14. Nuclei is blue (DAPI), and cytoskeleton is red (phalloidin). c) The cell counting kit-8 assay showing proliferation behavior of BMSCs seeded on FMSs at day 1, 4, and 7. d**)** The OM image of BMSCs-seeded FMSs (Ful 10) cultured at day 1, 4, 7, and 14. The FMSs morphology changes as the culture time prolongs (*e.g.* decreased transparency, blurred outline and fusion), indicating the increased amount of loaded cells. (n = 3, *, #, and $ indicate $p < 0.05$ in comparison with day 1, and day 4, respectively.).

μM of fullerol when compared to FMSs that contain 100 and 200 μM of fullerol at day three, which indicate the cytotoxicity of fullerol at the high dose. The BMSCs in Ful 0, Ful 1 and Ful 10 expanded well at day seven, and this almost covered the FMS surface at day 14. In contrast, the number of viable BMSCs in the Ful 100 and Ful 200 groups hardly increased at day 7 and 14, which might be the combined effect of cytotoxicity and cell differentiation. These results were also verified by F-actin staining, which mainly revealed the cell morphology and extension on FMSs at day 14 (Fig. 4b). Furthermore, the CCK-8 assay demonstrated that the proliferation activity of BMSCs was similar in the Ful 0, Ful 1 and Ful 10 groups, while this was significantly undermined in the Ful 100 and Ful 200 groups (Fig. 4c). In addition, the morphological changes of BMSCs seeded on FMSs (Ful 10) were also observed under the optical microscope (OM) at different culture times (Fig. 4d). The BMSCs were globosely and homogeneously suspended around the FMSs at day one, expanded and confluenced on FMSs at day 4 and 7, and spread out of FMSs at day 14. Obviously, the BMSCs on the FMSs proliferated over time with high viability. Furthermore, as the BMSCs proliferated and the amount of loaded cells increased, the morphological change of FMSs (*e.g.* decreased transparency, blurred outline, and fusion), was presented. These results showed that FMSs with certain dose fullerol (1 and 10 μM) are not cytotoxic, and could be used as promising carriers for BMSCs delivery.

### *3.4. FMSs protect BMSCs from oxidative stress damage under the ROS environment*

Excessive ROS in the tissue microenvironment cause oxidative stress to impair cellular functionalities, thereby causing various disorders [51]. In the case of refractory bone defects, the generated ROS (mainly $O2^-$, $H_2O_2$ and $OH^-$) at the lesion sites could induce oxidative stress damages to the host, as well as to the implant cells. According to the sources of ROS generation, the cellular localization of ROS quenching by fullerol is illustrated in Fig. 5a. In addition to the exogenous ROS from environment factors, the ROS were generated within cells at multiple sites, including the mitochondria, cytoplasm, endoplasmic reticulum, and plasma membrane, in which the mitochondria is not only the main source of intracellular ROS, but also the major target [52]. Specifically, intracellular ROS induces the depolarization of mitochondria, releasing pro-apoptotic molecules to cause cell apoptosis. In turn, mitochondrial depolarization promotes the ROS production with the activation of electron transfer, making the positive feedback for ROS generation. Pure GelMA microspheres exhibit a certain scavenging ability against hydroxyl radicals due to the presence of the hydroxyl groups [53]. However, their scavenging capacity against other forms of ROS remains limited. Fullerol is an excellent free-radical scavengers, which quenches ROS in a manner similar to biologically enzyme reactions [54]. In order to examine the scavenging ability of FMSs against extracellular ROS, the total antioxidant capability (TAOC) assay was conducted. The results indicated that the TOAC of FMSs was significantly enhanced with the increase in fullerol concentration: Ful 10 > Ful 1 > Control (Ful 0) (Fig. 5b). Next, the scavenging ability of FMSs against intracellular ROS was investigated *via* 2′,7′-dichlorodihydrofluorescein diacetate (DCFH-DA) oxidation. It is well known that nanomaterials, including fullerene [55,56], easily enter cells by endocytosis (receptor-mediated and/or direct penetration), and then are translocated into different organelles, thereby modulating the cell biological behaviors [57]. As illustrated in Fig. 5a, fullerol nanocrystals can enter into the stem cell,

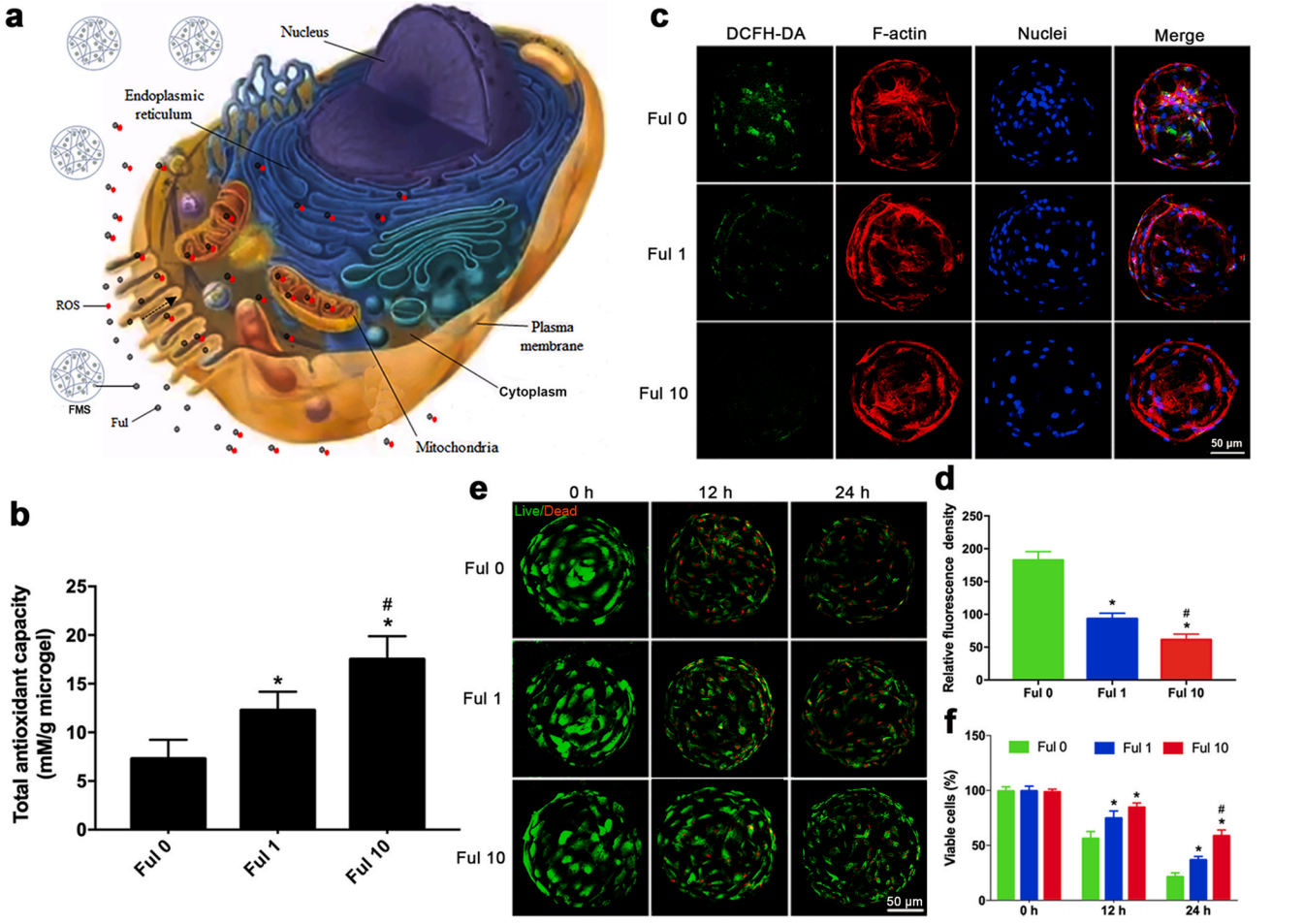


**Fig. 5.** Antioxidant activity of FMSs. a) An illustration of intracellular and extracellular ROS quenching by fullerol nanocrystals. The fullerol nanocrystals split from FSMs can, on the one hand, quench extracellular ROS, and on the other hand, enter into cells and eliminate the intracellular ROS. b)The total antioxidant capacity of pure FMSs without loading stem cells. c) Representative images of intracellular ROS (DCFH-DA) of BMSCs seeded on FMSs following $H_2O_2$ (100 μM) treatment for 2 h. d) Quantification analysis of DCFH-DA staining. e)The live/dead staining images of BMSCs seeded on FMSs following $H_2O_2$ (100 μM) treatment for 12 h and 24 h. 0 h refers to the baseline control without $H_2O_2$ treatment. f) Quantification analysis of viable cells. (n = 3, * and # indicate $p < 0.05$ in comparison with the Ful 0 group, and the Ful 1 group, respectively.)

and eliminated the intracellular ROS. It was shown that strong fluorescence (green) was observed in the Ful 0 group following $H_2O_2$ (100 μM) treatment for 2 h, indicating generation of large amounts of intracellular ROS. In contrast, the fluorescence intensity in Ful 1 and Ful 10 group significantly decreased, demonstrating the effective scavenging ability of FMSs against intracellular ROS (Fig. 5c). Likewise, the fluorescence intensity of DCFH-DA reduced with the enhancement of fullerol concentrations: Ful 10 > Ful 1 > Control (Ful 0) (Fig. 5d). Furthermore, after $H_2O_2$ (100 μM) treatment for 12 h, and 24 h, the cell survival of BMSCs was examined to investigate the ability of FMSs to rescue BMSCs under oxidative stress conditions (Fig. 5e and f). In the FMSs groups (Ful 1 and Ful 10), the BMSCs viabilities were significantly higher than those on the pure GelMA microspheres (Ful 0) group, and these were most obvious in the Ful 10 group under $H_2O_2$ treatment for 24 h. Taken together, these *in vitro* results demonstrated the robust scavenging ability of FMSs against both extracellular and intracellular ROS, which can be used to alleviate the oxidative stress in impaired tissue microenvironments, thereby improving the survival of implanted BMSCs.

### 3.5. FMSs promote the in vitro osteogenic differentiation of BMSCs via ROS-dependent and/or-independent signaling

Previous studies have demonstrated the link between oxidative stress and bone regeneration [58]. Oxidative stress suppresses osteogenic differentiation and antioxidants were supposed to promote osteogenesis. In order to investigate the effect of FMSs on osteogenesis, both calcium deposition and alkaline phosphatase (ALP) activity were evaluated. Initially, BMSCs-seeded FMSs were cultured in growth medium (GM) for 14 days, and the Alizarin Red S staining results revealed a slightly increase in mineralized matrix in the FMSs groups (Ful 10) (Figs. S4a and S4b). A similar effect was observed in the ALP activity assay when cultured for seven days (Figs. S4c and S4d). These demonstrated that FMSs (Ful 10) intrinsically exhibited an osteogenic property, which is superior to the pure fullerol aqueous solution [22], partly due to the optimized three-dimensional culture conditions, and the highly dispersed distribution of microfluidic fullerol nanocrystals. When cultured in osteogenic medium (OM), the osteogenesis was significantly enhanced. As shown in Fig. 6a, the mineralized matrix accumulating in the BMSCs-seeded FMSs deepened the color of FMSs under an optical microscope. The color of BMSCs-seeded FMSs was brown yellow at day 7 and turned to be tawny at day 14, indicating more generation of the mineralized matrix. Using Alizarin Red S staining, mineralized nodules were stained in red (Fig. 6b), which could be clearly observed under an optical microscope (Fig. 6c). The amount of mineralized matrix deposits increased with the culture time, and the fullerol concentration. It was observed that BMSCs seeded on FMSs (Ful 1 and Ful 10) had more mineralized nodules formations, when compared with that in the pure GelMA microspheres group (OM + Ful 0). The BMSCs-seeded GelMA

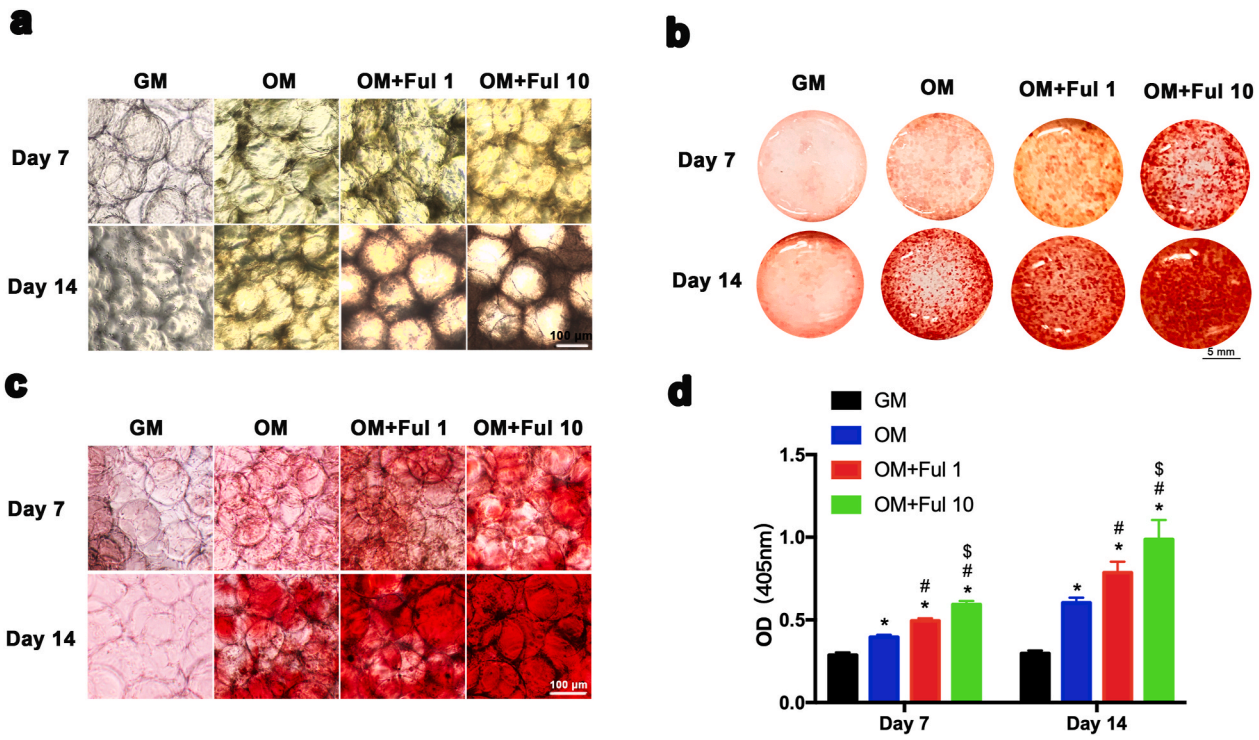


**Fig. 6.** The effect of FMSs on the formation of extracellular calcium nodule. The deeper the color, the more deposition of extracellular calcium nodule. a) Optical microscopic images of BMSC-laden FMSs in osteogenic medium at day 7 and 14. b) Overall photograph of BMSC-laden FMSs following Alizarin Red S staining at day 7 and 14. c) Optical microscopic images of BMSC-laden FMSs following Alizarin Red S staining at day 7 and 14. d) The quantification of calcium nodule in Alizarin red staining. (n = 3, *, #, and $ indicate $p < 0.05$ in comparison with the GM + Ful 0 group, the OM + Ful 0 group, and the OM + Ful 1 group, respectively.).

microspheres cultured in GM presented no mineralized nodules formation, which was used as a negative control. A consistent result was observed in the quantitation of the mineralized matrix. (Fig. 6d). Furthermore, ALP staining was performed for BMSCs-seeded FMSs at day 4 and day 7 (Fig. 7a and b). It was observed that the ALP expression was augmented as the culture periods was prolonged. The Ful 10 group had the highest ALP expression, followed by the Ful 1 group. A consistent trend was obtained in the quantitative analysis of the ALP activity (Fig. 7c). Taken together, these results demonstrated the excellent osteogenic property of FMSs, which can be used to promote the osteogenesis of BMSCs.

The representative molecules, *e.g.* ALP, COL1A1, OCN and *etc*, as the osteogenic-related markers, play an important role in the bone tissue regeneration, and have been widely investigated [22]. The expression of these osteocyte-specific genes and proteins were also measured to evaluate the osteoblast differentiation of BMSCs cultured on FMSs. As shown in Fig. 8b, the osteogenic differentiation-related genes, including ALP, COL1A1, OCN, BMP2, and RUNX2 were all significantly upregulated in the FMSs group (OM + Ful), when compared with that in GelMA microspheres group (OM), when cultured in OM for seven days. The genes expression of BMSCs cultured in GM was relatively lower and used as a negative control. In addition, the osteogenic-specific proteins (OCN, BMP2 and COL1A1) were also examined (Fig. 8a). The results revealed that BMSCs in GM seldom expressed these proteins, while the expressions were increased in OM. Similarly, the BMSCs seeded on FMSs presented with a significantly higher expression of osteogenic-specific proteins, when compared to that on GelMA microspheres.

In order to further clarify the underlying mechanism of FMSs to promote osteogenesis, the expression of several critical molecules was investigated. It is well known that excess ROS impairs the osteogenesis of the progenitor cells, and the targeting of ROS can be an effective strategy to change this process. To some extent, the antioxidative FMSs promote the osteogenesis of BMSCs by scavenging excessive ROS. However, the pathways that control mesenchymal cell differentiation are complex, and the molecular regulators of osteogenesis are not fully elucidated. For most cells, an increase in ROS stimulates a cell to upregulate antioxidant enzymes, such as SOD, and vice versa. This is the typical ROS-dependent pathway to resist oxidative stress. However, the self-protection capability of cells *via* this mechanism is limited, which can hardly resist the long-lasting oxidative stress with excessive ROS. For osteoblasts that exposed to long-lasting oxidative stress, there is another ROS-independent pathway to combat the oxidative stress, and this is different from that in other cells. Forkhead box O1 (FoxO1), which is a significant forkhead transcription factor, defends against ROS in osteoblasts *via* regulating superoxide dismutase 2 (SOD2) [59]. In addition, this promotes the osteoblast differentiation of stem cells by binding to RUNX2 [60]. A previous study has demonstrated that fullerol reinforces the osteogenesis of stem cells with the activation of the FoxO1 signaling pathway. In the present study, the expression of FoxO1 and SOD2 genes was analyzed (Fig. 8c). The results revealed that BMSCs cultured in GM presented with a lower expression of FoxO1 and SOD2, when compared to that cultured in OM. Specifically, the expression of FoxO1 and SOD2 in FMSs was significantly higher than that in GelMA microspheres. Consistent with the genes expression, a similar trend was obtained in the protein expression of FoxO1 and SOD2 (Fig. 8d), which further confirmed the positive role of FMSs on FoxO1 signaling. Taken together, these results preliminarily suggested that FMSs, with the activation of the FoxO1/SOD2 pathway, might promote the osteogenesis of BMSCs *via* ROS-dependent and/or-independent signaling (Scheme 1). Further investigations are needed to unveil the in-depth mechanism.

### 3.6. *BMSCs-laden FMSs promote in vivo bone healing in rat calvarial defects*

The bone healing effect of BMSCs-laden FMSs was evaluated in a rat calvarial defect model ($C_{Ful}$ = 10 μM, 0.035 wt% in respect to GelMA) (Fig. S5). BMSCs-laden FMSs were injected into calvarial defects with 24-gauge needles, and then the wounds were closed. At eight weeks

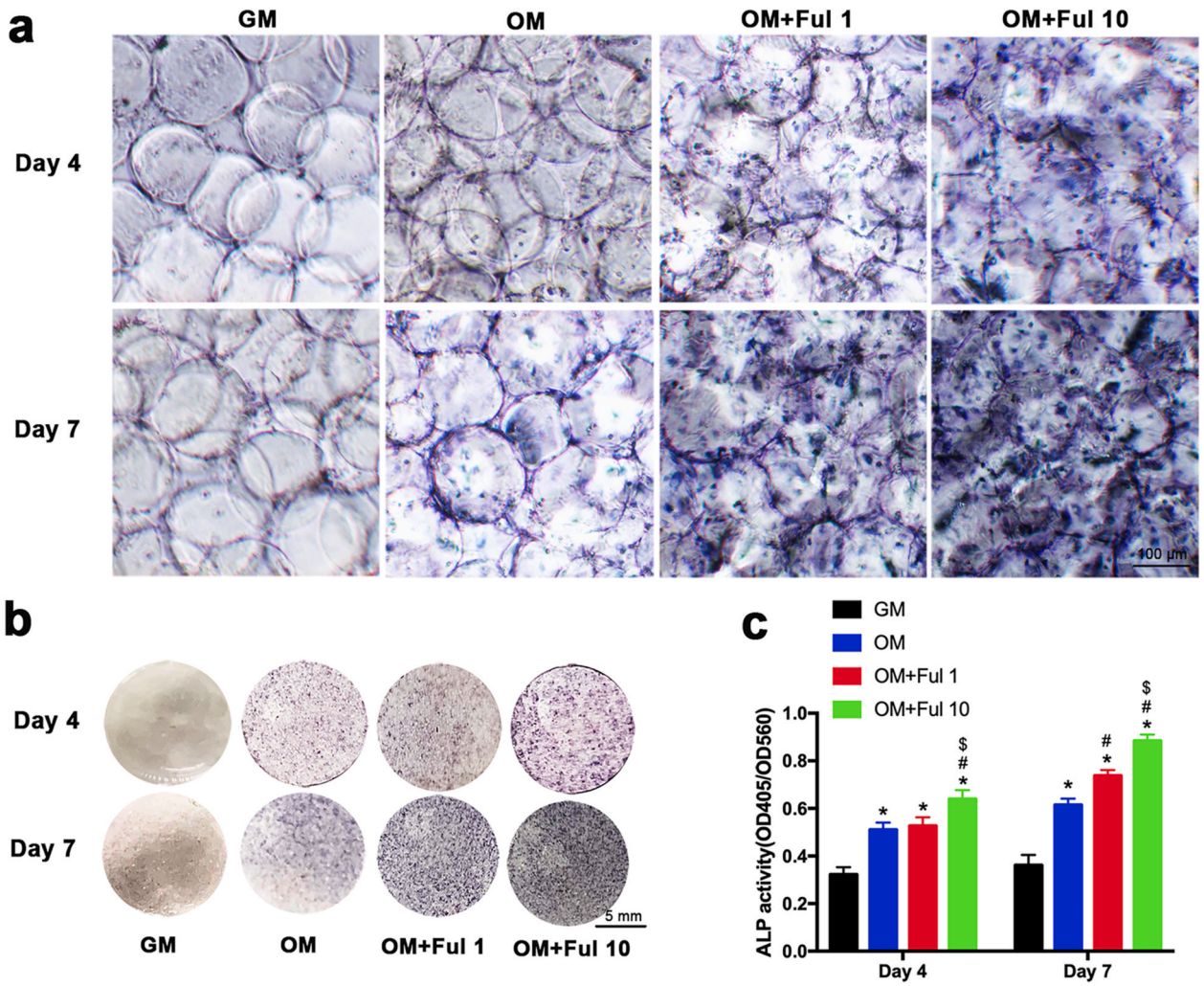


**Fig. 7.** The effect of FMSs on the ALP activity of BMSCs. **T**he deeper the color, the higher of ALP activity. a) Optical microscopic images of ALP staining of BMSCs-seeded FMSs in the osteogenic medium at day 4, and 7. b) Overall photograph of ALP staining of BMSC-laden FMSs in the osteogenic medium at day 4, and 7. c) The quantification of ALP activity in BMSCs. (n = 3, *, #, and $ indicate $p < 0.05$ in comparison with the GM group, the OM group, and the OM + Ful 1 group, respectively.).

post-surgery, the craniums were harvested and detected with Micro-CT and H&E staining, respectively. As shown in Fig. 9a, all the four groups presented with new bone formations, more or less, from the edge to the center, in the defect areas. The blank group was mostly empty in the defect area, although a small amount of new bone existed due to self-healing. In contrast, new bone formation significantly increased in the other groups, especially in the BMSCs-laden FMSs group. The bone volume (BV) fractions of the defect areas in the four groups were analyzed, and quantified in Fig. 9b. The BV fraction in the blank group was the lowest (4.1 ± 1.5%), when compared to the BMSCs group (12.6 ± 2.1%), GelMA + BMSCs group (23.7 ± 2.9%) and GelMA/Ful + BMSCs group (38.5 ± 2.8%), indicating the effective bone healing of BMSCs implantation. The BV fraction in the GelMA + BMSCs group was 1.89 fold of that in the BMSCs group, indicating the superiority of BMSCs-laden microspheres in the BMSCs implantation. This is partly due to the following: (i) the GelMA microspheres protect BMSCs from shear stress damage during the injection process, and (ii) provide sites for cell migration, adhesion and growth. Furthermore, the BV fractions in the GelMA/Ful + BMSCs group was 1.62-fold of that in the GelMA + BMSCs group, fully demonstrating the excellent *in vivo* bone healing effect of BMSCs-laden FMSs. These might be benefited from the following: (i) FMSs promote the osteogenesis of BMSCs to form new bones, and (ii) FMSs improve the impaired tissue microenvironment *via* scavenging excessive ROS, which is favorable for the survival of implant BMSCs and the self-healing of bone tissue. Consistent with BV fractures, a similar trend was observed for the bone mineral density (BMD) in the four groups (Fig. 9c). The H&E staining provides more detailed information of the repaired areas. The newly formed bone, fibrous tissue and blood vessel-like structure were shown in Fig. 10a. It can be observed that the calvarial defect areas in all groups had some newly formed bone, which is consistent with the results of the Micro-CT. Specifically, the defect areas in blank group were largely covered with fibrous tissues, and newly formed bone was only observed adjacent to the host bone. In comparison, more newly formed bone and blood-vessel-like structures were observed in the other three BMSCs implantation groups, indicating the better effect of bone tissue repair. Furthermore, the amount of newly formed bone in the GelMA/Ful + BMSCs group was the highest, followed by the GelMA + BMSCs group and BMSCs group. These results suggested that BMSCs-laden FMSs can significantly promote the *in vivo* bone healing in the defect areas.

In order to further verify the *in vivo* activation of osteogenic-related molecules during the bone healing process after the BMSCs-laden FMSs implantation, immunohistochemistry analysis was conducted in the defect areas of the four groups (Fig. 10b and c). The positive expression of proteins in the four groups was indicated by the blank arrows. It can be observed that the osteogenic-specific proteins, including OCN and

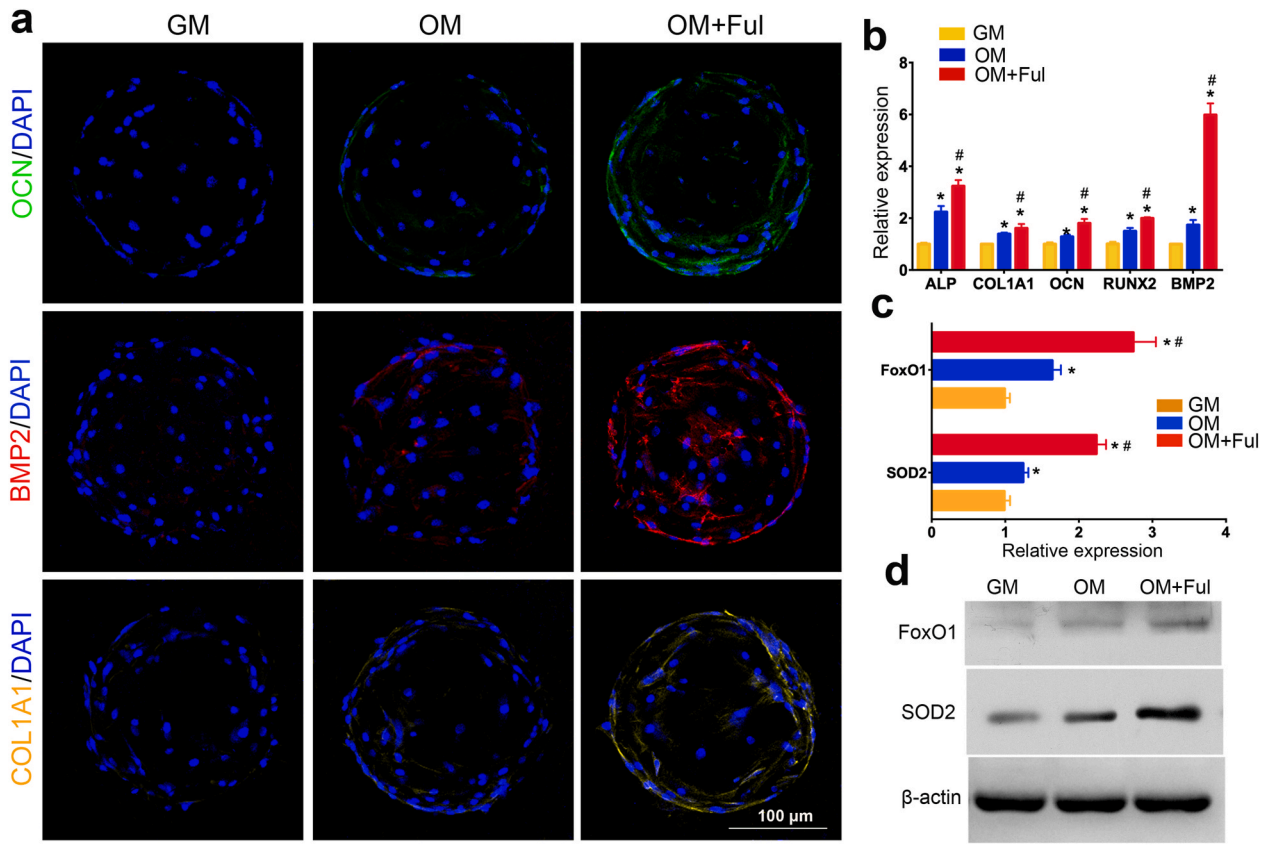


**Fig. 8.** The effect of FMSs on osteogenic molecule expression and FoxO1 signaling activation. a) LSCM images of fluorescently labelled OCN (green), BMP2 (red), and COL1A1(yellow) in BMSCs seeded on FMSs of for 7 days. b) qRT-PCR quantitative analysis of osteogenic genes, including alkaline phosphatase (ALP), collagen type I (COL1A1), runt-related transcription factor 2 (RUNX2), osteocalcin (OCN) and bone morphogenetic protein 2 (BMP2). c) qRT-PCR quantitative analysis of forkhead box O1 (FoxO1) and superoxide dismutase 2 (SOD2) in BMSCs seeded on FMSs for 7 days. d) Western blot images of FoxO1 and SOD2 in BMSCs seeded on FMSs for 7 days ($C_{Ful}$ = 10 μM, n = 3, *, and # indicate $p < 0.05$ in comparison with the GM group and the OM group, respectively.).

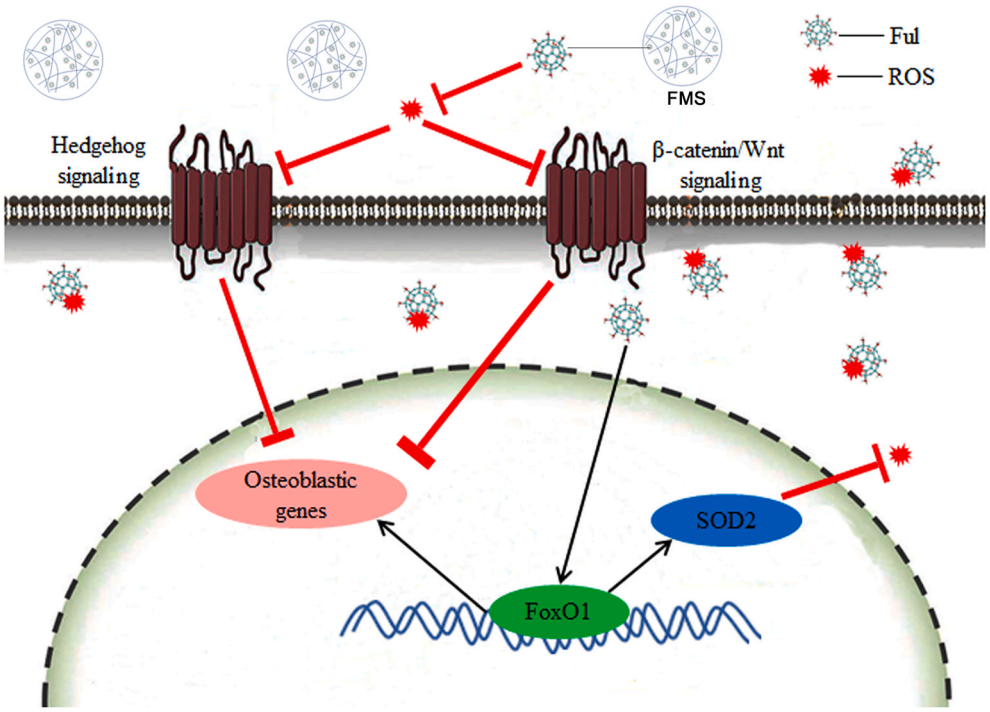


**Scheme 1.** Schematic of modulation of osteogenic differentiation of BMSCs on FMSs *via* regulating ROS-dependent and/or ROS-independent (FoxO1) signaling. The cell were seeded on FMSs, and the fullerol nanocrystals split from FMSs, on the one hand, can quench both the extracellular and intracellular ROS, thus to regulate the ROS-dependent signaling (*e.g.* Hedgehog signaling and β-catenin/Wnt signaling), and on the other hand, can directly enter cell to regulate the ROS-independent (FoxO1/SOD2) signaling.

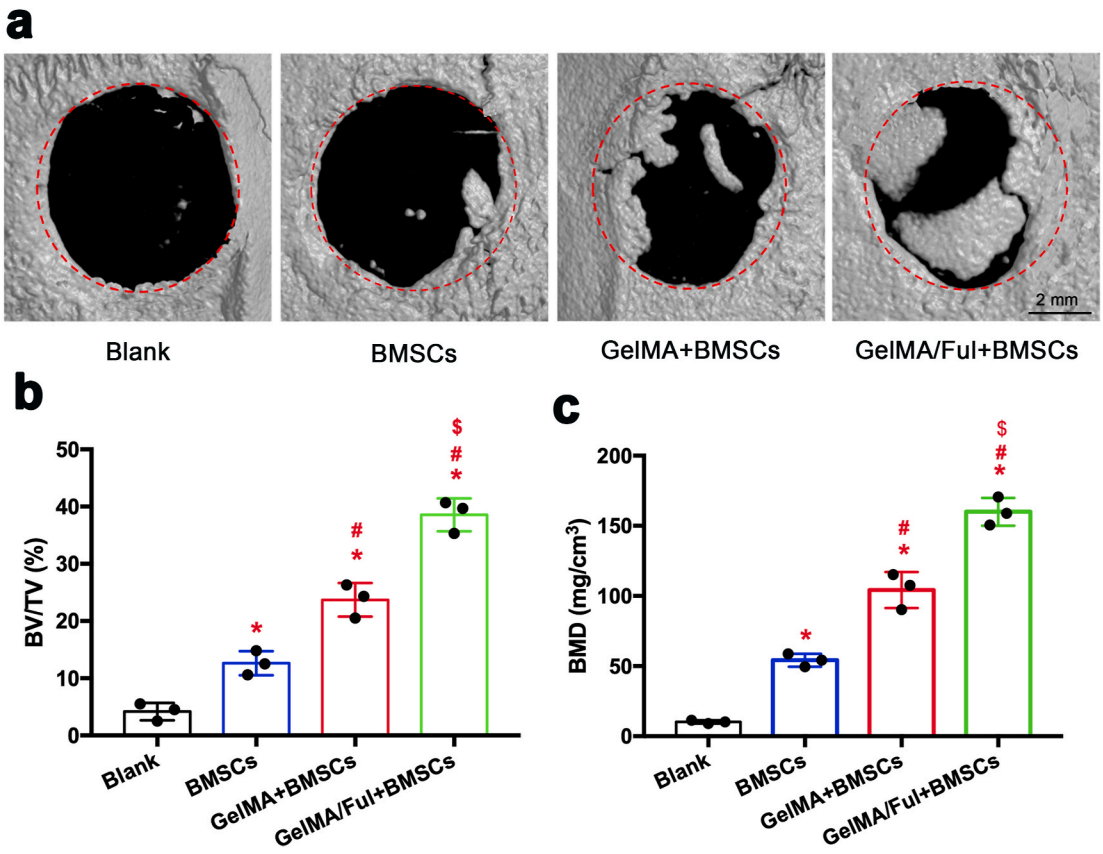


**Fig. 9.** Micro-CT evaluation of *in vivo* bone repair effect of BMSCs-laden FMSs. a) Micro-CT 3D-reconstructed images of new bone in the defect areas (circled by red dot line). b) Bone volume fraction (BV/TV), and c) Bone mineral density (BMD) of defect areas in different groups at week 8. ($C_{Ful}$ = 10 μM, n = 3, *, #, and $ indicate $p < 0.05$ in comparison with the blank group, the BMSCs group, and the GelMA + BMSCs group, respectively).

BMP2, were rarely expressed in the blank group, which were used as a negative control. The expression of BMP2 and OCN in the other three groups was much higher than that in the blank group, which was consistent with the results of the radiological and histological evaluation. The BMSCs-laden FMSs group presented with the strongest expression of OCN and BMP2 in terms of both areas and density, which further verify the robust bone healing effect of this system. Furthermore, the *in vivo* activation of FoxO1 signaling, which is a major pathway that resists oxidative stress in bone tissue [61], was investigated after FMSs implantation. The expression of FoxO1 and SOD2 in the blank group was relatively low, which was enhanced by BMSCs implantation in the other three groups, suggesting that the stem cell itself might improve the oxidative stress microenvironment to some extent [62]. Although the expression of FoxO1 and SOD2 in the BMSCs and GelMA + BMSCs group was higher, when compared to the blank group, this was relatively lower, when compared with the GelMA/Ful + BMSCs group, indicating the great potential of FMSs in defending against *in vivo* ROS.

Taken together, these results demonstrated that BMSCs-laden FMSs are able to effectively repair the *in vivo* bone defect *via* modulating the ROS microenvironment to promote the osteogenesis of BMSCs, and this is consistent with *in vitro* results, indicating a promising strategy for refractory bone healing. It should be noted that the stem cells used in the study were allogeneic. However, further studies should investigate the effectiveness and feasibility of this system using more sources of stem cells (both the autologous and allogeneic) in large animals (*e.g.* dog) before the final clinical investigation [63]. Compared to the application *via* intravenous injection, the systemic toxicity of fullerol was almost negligible in the local application of FMSs, since most of the fullerol was confined in the bone tissue, and was finally cleared by the mononuclear phagocyte system [64].

## 4. Conclusions

In summary, this work demonstrates a facile and efficient approach to prepare uniform, particle-size controllable FMSs that contain highly dispersed fullerol nanocrystals using an one-step innovational microfluidic technology for the *in situ* redox regulation of stem cell fate and refractory bone healing. These FMSs could effectively quench ROS to protect BMSCs from oxidative stress damage, providing a favorable condition for their survival during the process of deposition. In addition, the bioactive FMSs exhibited robust capability to promote the osteoblast differentiation of BMSCs *via* ROS-dependent and/or ROS-independent signaling pathways. More importantly, compared with BMSCs-laden GelMA microspheres, BMSCs-laden FMSs could significantly reinforce the *in vivo* bone healing with the activation of FoxO1 signaling, which should be a synergistic effect that result from (i) FMSs in improving the survival of BMSCs (both implanted and resident) *via* scavenging excessive ROS in the refractory bone defects, and (ii) FMSs in promoting the osteogenesis of BMSCs. Overall, these modular FMSs that target the ROS microenvironment have enormous potential as injectable delivery vehicles of BMSCs for refractory bone healing, and this can also be expanded to deliver a variety of other cells, targeting diseases that require *in situ* redox regulation.

## Data availability

The data that support this study are available within the article and its Supplementary data files are available from the authors upon request.

## CRediT authorship contribution statement

**Jielai Yang:** Conceptualization, Investigation, Methodology,

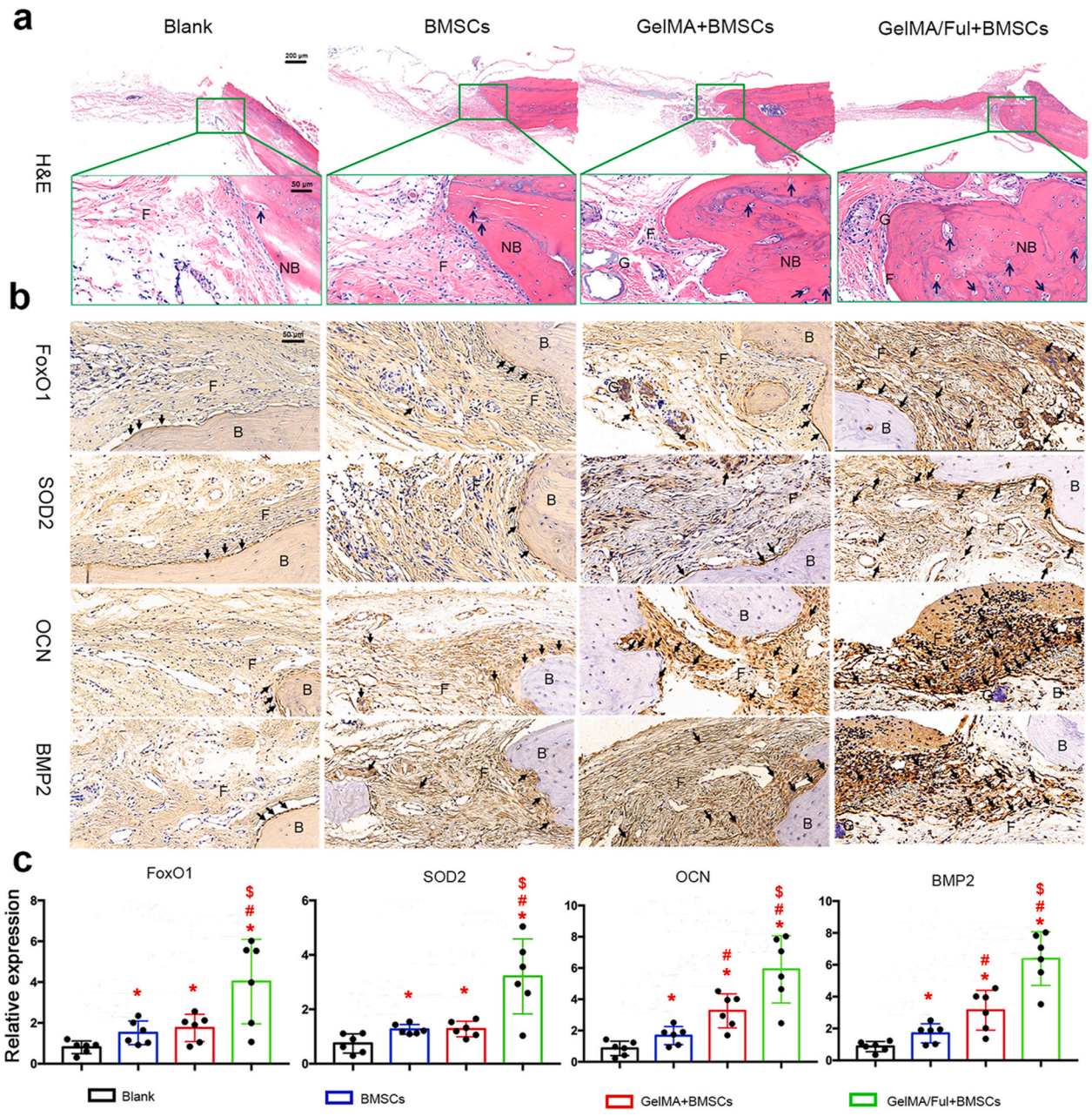


**Fig. 10.** Histomorphological evaluation of *in vivo* bone repair effect of BMSCs-loaded FMSs. a) Representative images of defect area in cranium using H&E staining. Fibrous tissue (F), new bone (NB), GelMA hydrogel (G) and blood vessel-like structure (black arrow) are indicated in the selected section. b) Representative immunohistochemical images in decalcified bone defect area showing the expression of FoxO1, SOD2, OCN and BMP2 in each group. Fibrous tissue (F), Bone (B), GelMA hydrogel (G) and positive-expressed protein (black arrow) are indicated in the selected section. c) Semi-quantitative analysis of the expression of FoxO1, SOD2, OCN and BMP2 in each group. ($C_{Ful}$ = 10 μM, n = 6, *, #, and $ indicate $p < 0.05$ in comparison with the blank group, the BMSCs group, and the GelMA + BMSCs group, respectively).

Writing – original draft. **Jing Liang:** Investigation, Data curation. **Yuan Zhu:** Data curation, Software. **Mu Hu:** Software, Methodology. **Lianfu Deng:** Project administration, Visualization. **Wenguo Cui:** Writing – review & editing, Funding acquisition. **Xiangyang Xu:** Supervision, Funding acquisition, Validation.

## Declaration of competing interest

The authors declare no conflict of interest.

## Acknowledgements

This work was supported by the National Key Research and Development Program of China (2020YFA0908200), National Natural Science Foundation of China (81772372 and 81930051), Shanghai Jiao Tong University "Medical and Research" Program (ZH2018ZDA04), Science and Technology Commission of Shanghai Municipality (18140901500,19440760400) and Shanghai Municipal Health and Family Planning Commission (201840027).

## Appendix A. Supplementary data

Supplementary data to this article can be found online at https://doi.org/10.1016/j.bioactmat.2021.05.024.

## References


[1] R.H. Haralson 3rd, J.D. Zuckerman, Prevalence, health care expenditures, and orthopedic surgery workforce for musculoskeletal conditions, J. Am. Med. Assoc. 302 (2009) 1586–1587.

[2] H. Jiao, E. Xiao, D.T. Graves, Diabetes and its effect on bone and fracture healing, Curr. Osteoporos. Rep. 13 (2015) 327–335.

[3] M. Valko, D. Leibfritz, J. Moncol, M.T. Cronin, M. Mazur, J. Telser, Free radicals and antioxidants in normal physiological functions and human disease, Int. J. Biochem. Cell Biol. 39 (2007) 44–84.

[4] R. Siddappa, H. Fernandes, J. Liu, C. van Blitterswijk, J. de Boer, The response of human mesenchymal stem cells to osteogenic signals and its impact on bone tissue engineering, Curr. Stem Cell Res. Ther. 2 (2007) 209–220.

[5] A.C. Daly, L. Riley, T. Segura, J.A. Burdick, Hydrogel microparticles for biomedical applications, Nat. Rev. Mater. 5 (2020) 1–24.

[6] T. Kaully, K. Kaufman-Francis, A. Lesman, S. Levenberg, Vascularization–The conduit to viable engineered tissues, Tissue Eng. B Rev. 15 (2009) 159–169.

[7] B.D. Sui, C.H. Hu, A.Q. Liu, C.X. Zheng, K. Xuan, Y. Jin, Stem cell-based bone regeneration in diseased microenvironments: challenges and solutions, Biomaterials 196 (2019) 18–30.

[8] T. Hao, J. Li, F. Yao, D. Dong, Y. Wang, B. Yang, C. Wang, Injectable fullerenol/alginate hydrogel for suppression of oxidative stress damage in Brown adipose-derived stem cells and cardiac repair, ACS Nano 11 (2017) 5474–5488.

[9] A. Sandukji, H. Al-Sawaf, A. Mohamadin, Y. Alrashidi, S.A. Sheweita, Oxidative stress and bone markers in plasma of patients with long-bone fixative surgery: role of antioxidants, Hum. Exp. Toxicol. 30 (2011) 435–442.

[10] P. Thoniyot, M.J. Tan, A.A. Karim, D.J. Young, X.J. Loh, Nanoparticle-hydrogel composites: concept, design, and applications of these promising, multi-functional materials, Adv. Sci. 2 (2015), 1400010.

[11] K. Yue, G. Trujillo-de Santiago, M.M. Alvarez, A. Tamayol, N. Annabi, A. Khademhosseini, Synthesis, properties, and biomedical applications of gelatin methacryloyl (GelMA) hydrogels, Biomaterials 73 (2015) 254–271.

[12] B.J. Klotz, D. Gawlitta, A. Rosenberg, J. Malda, F.P.W. Melchels, Gelatin-methacryloyl hydrogels: towards biofabrication-based tissue repair, Trends Biotechnol. 34 (2016) 394–407.

[13] J. Grebowski, P. Kazmierska, A. Krokosz, Fullerenols as a new therapeutic approach in nanomedicine, BioMed Res. Int. 2013 (2013), 751913.

[14] R. Injac, M. Prijatelj, B. Strukelj, Fullerenol nanoparticles: toxicity and antioxidant activity, Methods Mol. Biol. 1028 (2013) 75–100.

[15] E.E. Fileti, R. Rivelino, F. Brito Mota, T. Malaspina, Effects of hydroxyl group distribution on the reactivity, stability and optical properties of fullerenols, Nanotechnology 19 (2008), 365703.

[16] S. Osuna, M. Swart, M. Sola, On the mechanism of action of fullerene derivatives in superoxide dismutation, Chemistry 16 (2010) 3207–3214.

[17] N. Tsao, T.Y. Luh, C.K. Chou, J.J. Wu, Y.S. Lin, H.Y. Lei, Inhibition of group A streptococcus infection by carboxyfullerene, Antimicrob. Agents Chemother. 45 (2001) 1788–1793.

[18] J. Tang, R. Zhang, M. Guo, L. Shao, Y. Liu, Y. Zhao, S. Zhang, Y. Wu, C. Chen, Nucleosome-inspired nanocarrier obtains encapsulation efficiency enhancement and side effects reduction in chemotherapy by using fullerenol assembled with doxorubicin, Biomaterials 167 (2018) 205–215.

[19] M. Seke, D. Petrovic, A. Djordjevic, D. Jovic, M.L. Borovic, Z. Kanacki, M. Jankovic, Fullerenol/doxorubicin nanocomposite mitigates acute oxidative stress and modulates apoptosis in myocardial tissue, Nanotechnology 27 (2016), 485101.

[20] X. Yang, L. Jin, L. Yao, F.H. Shen, A.L. Shimer, X. Li, Antioxidative nanofullerol prevents intervertebral disk degeneration, Int. J. Nanomed. 9 (2014) 2419–2430.

[21] K. Yudoh, K. Shishido, H. Murayama, M. Yano, K. Matsubayashi, H. Takada, H. Nakamura, K. Masuko, T. Kato, K. Nishioka, Water-soluble C60 fullerene prevents degeneration of articular cartilage in osteoarthritis *via* down-regulation of chondrocyte catabolic activity and inhibition of cartilage degeneration during disease development, Arthritis Rheum. 56 (2007) 3307–3318.

[22] X. Yang, C.J. Li, Y. Wan, P. Smith, G. Shang, Q. Cui, Antioxidative fullerol promotes osteogenesis of human adipose-derived stem cells, Int. J. Nanomed. 9 (2014) 4023–4031.

[23] H. Geng, Y.N. Chang, X. Bai, S. Liu, Q. Yuan, W. Gu, J. Li, K. Chen, G. Xing, G. Xing, Fullerenol nanoparticles suppress RANKL-induced osteoclastogenesis by inhibiting differentiation and maturation, Nanoscale 9 (2017) 12516–12523.

[24] K. Kokubo, S. Shirakawa, N. Kobayashi, H. Aoshima, T. Oshima, Facile and scalable synthesis of a highly hydroxylated water-soluble fullerenol as a single nanoparticle, Nano Res 4 (2011) 204–215.

[25] V. Georgakilas, F. Pellarini, M. Prato, D.M. Guldi, M. Melle-Franco, F. Zerbetto, Supramolecular self-assembled fullerene nanostructures, Proc. Natl. Acad. Sci. U.S.A. 99 (2002) 5075–5080.

[26] E.M. Hotze, J.Y. Bottero, M.R. Wiesner, Theoretical framework for nanoparticle reactivity as a function of aggregation state, Langmuir 26 (2010) 11170–11175.

[27] M. Chen, et al., Aggregation behavior and antioxidant properties of amphiphilic fullerene C60 derivatives cofunctionalized with cationic and nonionic hydrophilic groups, Langmuir 35 (2019) 6939–6949.

[28] S.N. Bhatia, U.J. Balis, M.L. Yarmush, M. Toner, Effect of cell-cell interactions in preservation of cellular phenotype: cocultivation of hepatocytes and nonparenchymal cells, Faseb. J. 13 (1999) 1883–1900.

[29] E.P. Herrero, E.M. Del Valle, M.A. Galan, Immobilization of mesenchymal stem cells and monocytes in biocompatible microcapsules to cell therapy, Biotechnol. Prog. 23 (2007) 940–945.

[30] Z. Liu, F. Fontana, A. Python, J.T. Hirvonen, H.A. Santos, Microfluidics for production of particles: mechanism, methodology, and applications, Small 16 (2019), 1904673.

[31] Y. Song, J. Hormes, C.S. Kumar, Microfluidic synthesis of nanomaterials, Small 4 (2008) 698–711.

[32] P.M. Valencia, O.C. Farokhzad, R. Karnik, R. Langer, Microfluidic technologies for accelerating the clinical translation of nanoparticles, Nat. Nanotechnol. 7 (2012) 623–629.

[33] W. Jiang, M. Li, Z. Chen, K.W. Leong, Cell-laden microfluidic microgels for tissue regeneration, Lab Chip 16 (2016) 4482–4506.

[34] C. Cha, J. Oh, K. Kim, Y. Qiu, M. Joh, S.R. Shin, X. Wang, G. Camci-Unal, K.T. Wan, R. Liao, A. Khademhosseini, Microfluidics-assisted fabrication of gelatin-silica core-shell microgels for injectable tissue constructs, Biomacromolecules 15 (2014) 283–290.

[35] S.R. Shin, H. Bae, J.M. Cha, J.Y. Mun, Y.C. Chen, H. Tekin, H. Shin, S. Farshchi, M. R. Dokmeci, S. Tang, A. Khademhosseini, Carbon nanotube reinforced hybrid microgels as scaffold materials for cell encapsulation, ACS Nano 6 (2012) 362–372.

[36] J.L. Yang, Y. Zhu, F. Wang, L.F. Deng, X.Y. Xu, W.G. Cui, Microfluidic liposomes-anchored microgels as extended delivery platform for treatment of osteoarthritis, Chem. Eng. J. 400 (2020), 126004.

[37] M. Inoue, G. Kratz, A. Haegerstrand, M. Stahle-Backdahl, Collagenase expression is rapidly induced in wound-edge keratinocytes after acute injury in human skin, persists during healing, and stops at re-epithelialization, J. Invest. Dermatol. 104 (1995) 479–483.

[38] G. Ghiacci, G. Graiani, F. Ravanetti, S. Lumetti, E. Manfredi, C. Galli, A. Cacchioli, G.M. Macaluso, R. Sala, Over-inlay" block graft and differential morphometry: a novel block graft model to study bone regeneration and host-to-graft interfaces in rats, J. Periodontal Implant Sci. 46 (2016) 220–233.

[39] X. Zhao, S. Liu, L. Yildirimer, H. Zhao, R. Ding, H. Wang, W. Cui, D. Weitz, Injectable stem cell-laden photocrosslinkable microspheres fabricated using microfluidics for rapid generation of osteogenic tissue constructs, Adv. Funct. Mater. 26 (2016) 2809–2819.

[40] A.K. Chen, S. Reuveny, S.K. Oh, Application of human mesenchymal and pluripotent stem cell microcarrier cultures in cellular therapy: achievements and future direction, Biotechnol. Adv. 31 (2013) 1032–1046.

[41] H. Tavassoli, S.N. Alhosseini, A. Tay, P.P. Chan, S.K.W. Oh, M.E. Warkiani, Large-scale production of stem cells utilizing microcarriers: a biomaterials engineering perspective from academic research to commercialized products, Biomaterials 181 (2018) 333–346.

[42] G. Zhang, Y. Liu, D. Liang, L. Gan, Y. Li, Facile synthesis of isomerically pure fullerenols and formation of spherical aggregates from C60(OH)8, Angew Chem. Int. Ed. Engl. 49 (2010) 5293–5295.

[43] J.A. Brant, J. Labille, C.O. Robichaud, M. Wiesner, Fullerol cluster formation in aqueous solutions: implications for environmental release, J. Colloid Interface Sci. 314 (2007) 281–288.

[44] J.A. Brant, J. Labille, J.Y. Bottero, M.R. Wiesner, Characterizing the impact of preparation method on fullerene cluster structure and chemistry, Langmuir 22 (2006) 3878–3885.

[45] Y. Jiang, N. Krishnan, J. Heo, R.H. Fang, L. Zhang, Nanoparticle-hydrogel superstructures for biomedical applications, J. Contr. Release 324 (2020) 505–521.

[46] K. Kokubo, K. Matsubayashi, H. Tategaki, H. Takada, T. Oshima, Facile synthesis of highly water-soluble fullerenes more than half-covered by hydroxyl groups, ACS Nano 2 (2008) 327–333.

[47] N.T. Thanh, N. Maclean, S. Mahiddine, Mechanisms of nucleation and growth of nanoparticles in solution, Chem. Rev. 114 (2014) 7610–7630.

[48] Y. Su, J.Y. Xu, P. Shen, J. Li, L. Wang, Q. Li, W. Li, G.T. Xu, C. Fan, Q. Huang, Cellular uptake and cytotoxic evaluation of fullerenol in different cell lines, Toxicology 269 (2010) 155–159.

[49] C.M. Sayes, J.D. Fortner, W. Guo, D. Lyon, A.M. Boyd, K.D. Ausman, Y.J. Tao, B. Sitharaman, L.J. Wilson, J.B. Hughes, The differential cytotoxicity of water-soluble fullerenes, Nano Lett. 4 (2004) 1881–1887.

[50] N. Lewinski, V. Colvin, R. Drezek, Cytotoxicity of nanoparticles, Small 4 (2008) 26–49.

[51] S. Joshi-Barr, C. de Gracia Lux, E. Mahmoud, A. Almutairi, Exploiting oxidative microenvironments in the body as triggers for drug delivery systems, Antioxidants Redox Signal. 21 (2014) 730–754.

[52] F. Wauquier, L. Leotoing, V. Coxam, J. Guicheux, Y. Wittrant, Oxidative stress in bone remodelling and disease, Trends Mol. Med. 15 (2009) 468–477.

[53] E. Mendis, N. Rajapakse, S.-K. Kim, Antioxidant properties of a radical-scavenging peptide purified from enzymatically prepared fish skin gelatin hydrolysate, J. Agric. Food Chem. 53 (2005) 581–587.

[54] P. Anilkumar, F. Lu, L. Cao, P.G. Luo, J.-H. Liu, S. Sahu, K. N Tackett II, Y. Wang, Y.-P. Sun, Fullerenes for applications in biology and medicine, Curr. Med. Chem. 18 (2011) 2045–2059.

[55] T. Hao, J. Zhou, S. Lü, B. Yang, Y. Wang, W. Fang, X. Jiang, Q. Lin, J. Li, C. Wang, Fullerene mediates proliferation and cardiomyogenic differentiation of adipose-derived stem cells *via* modulation of MAPK pathway and cardiac protein expression, Int. J. Nanomed. 11 (2016) 269–283.

[56] F. Lao, L. Chen, W. Li, C. Ge, Y. Qu, Q. Sun, Y. Zhao, D. Han, C. Chen, Fullerene nanoparticles selectively enter oxidation-damaged cerebral microvessel endothelial cells and inhibit JNK-related apoptosis, ACS Nano 3 (2009) 3358–3368.

[57] L.C. Cheng, X. Jiang, J. Wang, C. Chen, R.S. Liu, Nano-bio effects: interaction of nanomaterials with cells, Nanoscale 5 (2013) 3547–3569.

[58] F. Atashi, A. Modarressi, M.S. Pepper, The role of reactive oxygen species in mesenchymal stem cell adipogenic and osteogenic differentiation: a review, Stem Cell. Dev. 24 (2015) 1150–1163.
[59] M.T. Rached, A. Kode, L. Xu, Y. Yoshikawa, J.H. Paik, R.A. Depinho, S. Kousteni, FoxO1 is a positive regulator of bone formation by favoring protein synthesis and resistance to oxidative stress in osteoblasts, Cell Metabol. 11 (2010) 147–160.
[60] C.C. Teixeira, Y. Liu, L.M. Thant, J. Pang, G. Palmer, M. Alikhani, Foxo1, a novel regulator of osteoblast differentiation and skeletogenesis, J. Biol. Chem. 285 (2010) 31055–31065.
[61] Y. Zhang, Y. Xiong, J. Zhou, N. Xin, Z. Zhu, Y. Wu, FoxO1 expression in osteoblasts modulates bone formation through resistance to oxidative stress in mice, Biochem. Biophys. Res. Commun. 503 (2018) 1401–1408.
[62] X. Teng, L. Chen, W. Chen, J. Yang, Z. Yang, Z. Shen, Mesenchymal stem cell-derived exosomes improve the microenvironment of infarcted myocardium contributing to angiogenesis and anti-inflammation, Cell. Physiol. Biochem. 37 (2015) 2415–2424.
[63] K.H. Kraus, C. Kirker-Head, Mesenchymal stem cells and bone regeneration, Vet. Surg. 35 (2006) 232–342.
[64] J.P. Almeida, A.L. Chen, A. Foster, R. Drezek, In *Vivo* biodistribution of nanoparticles, Nanomedicine 6 (2011) 815–835.